High-resolution simulations of cylindrical void collapse in energetic materials: Effect of primary and secondary collapse on initiation thresholds

Nirmal Kumar Rai, Martin J. Schmidt, and H. S. Udaykumar

Phys. Rev. Fluids **2**, 043202 — Published 28 April 2017

DOI: 10.1103/PhysRevFluids.2.043202

High resolution simulations of cylindrical void collapse in energetic materials: Effect of primary and secondary collapse on initiation thresholds

Nirmal Kumar Rai[1], Martin J Schmidt[2] and H. S. Udaykumar[1,*]

[1]Department of Mechanical and Industrial Engineering, The University of Iowa, Iowa City, IA-52242, USA

[2]AFRL-RW, Eglin Air Force Base, Florida 32542, USA

ABSTRACT

Void collapse in energetic materials leads to hot spot formation and enhanced sensitivity. Much recent work has been directed towards simulation of collapse-generated reactive hot spots. The resolution of voids in calculations to date have varied as have the resulting predictions of hot spot intensity. Here we first determine the required resolution for reliable cylindrical void collapse calculations leading to initiation of chemical reactions. High resolution simulations of collapse provide new insights into the mechanism of hot spot generation. It is found that initiation can occur in two different modes depending on the loading intensity: either the initiation occurs due to jet impact at the first collapse instant or it can occur at secondary lobes at the periphery of the collapsed void. A key observation is that secondary lobe collapse leads to large local temperatures that initiate reactions. This is due to a combination of a strong blast wave from the site of primary void collapse and strong colliding jets and vortical flows generated during the collapse of the secondary lobes. The secondary lobe collapse results in a significant lowering of the predicted threshold for ignition of the energetic material. The results suggest that meso-scale simulations of void fields may suffer from significant uncertainty in threshold predictions because unresolved calculations cannot capture the secondary lobe collapse phenomenon. The implications of this uncertainty for meso-scale simulations are discussed in this paper.

Keywords: *Void Collapse, Pore Collapse, HMX, Shock initiation, Porous energetic materials, Meso-scale Simulations.*

I. INTRODUCTION

Prediction of initiation sensitivity of energetic materials is important to enhance and control their ignition and detonation characteristics. Initiation of such materials is thought to occur at hot spots that are generated by a variety of mechanisms [1]. Collapse of voids in a porous energetic material is one important mechanism for initiation via hot spots [1–4]. Experimental work on heterogeneous explosives indicates a strong link between porosity and initiation sensitivity [5]. To gain physical insight into the void collapse generated hot spot mechanism and to model and predict sensitivity of porous explosives, simulations of void collapse are increasingly employed. Both inert [6–10] and reactive [11–13] void collapse simulations have been performed. Previous simulations [6–8,10–12,14] of void collapse have used a wide range of grid resolutions but no *a priori* guideline on the adequacy of the grid resolution exists in the literature. Here we examine the issue of grid resolution and its impact on initiation predictions from reactive void collapse simulations. Grid resolution is shown to play an important role in determining the local temperature rise and the location of maximum temperature following void collapse. By performing high resolution simulations new insights are obtained on the physics of void collapse and hot spot generation. The findings reported herein carry important implications for initiation threshold prediction in energetic materials.

The study of void collapse in porous energetic materials has been an active area of research [2–4,6,7,9–12,15]. Previous studies have discussed various aspects of the collapse mechanism via physical experiments [2–4], molecular dynamics (MD) simulations [16,17] and continuum level meso-scale simulations [6–12,15]. A notable experimental work is the one by Swantek et al. [2] on the impact induced collapse of cylindrical voids in a mixture of agarose and glycerol. Swantek et al. [2] performed void collapse experiments on a single cylindrical void, two voids and a staggered array of 4 voids. The study provided important quantitative data on the mechanics of void collapse in the transparent medium although it was restricted to planar voids and to an inert material. The formation of material jets was observed along with asymmetrical void collapse. Also, the collapse of an array of voids revealed collapse inhibiting and collapse triggering situations depending on the relative void positioning.

Experiments by Bourne et al. [4] on void collapse in liquid nitromethane also provided important insights on the collapse of cylindrical voids in energetic materials. Bourne et al. [4] reported on the formation of a material jet upon the deformation of the front surface of the void (see illustration in Figure 1). This material jet impacts the rear surface and high temperature is achieved. In Bourne et al. [4] experiments the high temperature is indicated via a first bright flash near the jet impact site. The jet impact forms two symmetrical lobes of gas pockets and the subsequent collapse of these two lobes causes further rise in temperature. The two symmetrical pockets of secondary lobes collapse under the influence of the primary blast wave emanating from the initial jet impact. The temperature reached in these two lobes during collapse is reported to be *higher* than the initial jet impact temperature. Bourne et al. [4] concluded that the primary jet impact site is the most likely ignition site, although the temperature reached in the secondary lobes are high. They argue that this is because the secondary heated regions exist for a very small duration of time and the temperature reached at the primary jet impact site is in any case sufficient enough to initiate reaction. These conclusions however may apply only to the limited parameter range in which the experiments were conducted.

The experimental studies have provided important insights into the physics of void collapse of millimeter-sized voids. However, in real samples the size of the voids may vary from nanometers to millimeters. Recent MD efforts [16,17] have shed light on the physics of nanometer-sized void collapse. Eason and Sewell [16] have discussed the effect of shock loading on a $35\,nm$ cylindrical void present in RDX. Weak to high shock strengths i.e. $1-3\,km/s$ shock have been used to study the effect of the loading conditions. The collapse features have been shown to vary greatly with the loading conditions. They show that material jetting is not observed for the weaker shocks but as the strength of the shock is increased the jetting and focusing increases. Also, jetting causes the formation of rotational velocity fields following collapse. The rotational velocity field transports the kinetic energy and redistributes it away from the initial collapse region. The recent MD work of Zhou et al. [17] on void collapse in HMX also reveals interesting void collapse physics. Cylindrical voids of various sizes from $2-5\,nm$ radius were used in the study under the shock load of $0.5-3\ km/s$. The results are shown to be agreement with the work of Eason and Sewell [16] in terms of the collapse behavior under different shock regimes. It is shown that for the higher shock strength, a secondary hot conical region is formed after the initial jet impact. The secondary hot region is formed because of the recompression of the material by the strong shock wave generated from the initial jet impact. This secondary compression was not observed for the weaker shocks.

Apart from experiments and MD simulations, various attempts have been made to study the void collapse phenomenon numerically via meso-scale simulations [6–9,11,12,14]. The early work by Menikoff [6] provides interesting insights into the phenomenon of void collapse and the involvement of dissipative phenomena such as viscous dissipation and plastic work in the formation of hot spots. However, the void collapse results shown in the work of Menikoff contradicts some aspects of the experimental findings of Bourne et al. [4]. While the overall aspects of the initial jet impact are captured, the formation of heated secondary lobes that are seen in the experiments of Bourne et al. [4] was not observed in Menikoff's [6] simulations. Instead, the gas cavity formed after the jet impact does not fully collapse under the influence of the primary blast wave. The gas lobes formed in the secondary void structure are in fact calculated to be at a lower temperature than the primary jet impact temperature in the work of Menikoff [6]. In the present work these discrepancies between Bourne et al. [4] and Menikoff's [6] calculations will be analyzed. The reason for this discrepancy will be shown to arise perhaps from the inadequate resolution of voids in the calculations by Menikoff [6].

Void collapse leading to hot spot formation and initiation of reaction was analyzed in the work of Tran et al. [11] where HMX decomposition was modeled using the Tarver [18] 4-equation chemical kinetic mechanism for HMX. The effect of void size and loading intensity on energy deposition in HMX was also demonstrated. However, Tran et al. [11] did not establish a grid refinement criterion that can be used in the void collapse simulations. The work by Kapahi and Udaykumar [8] on the study of cylindrical void collapse discusses the different stages involved in the void collapse process. It is shown that the different stages are governed by different physical mechanisms such as plastic dissipation, material jetting and the conversion of kinetic energy of the jet to internal energy. The effects of void-void interactions were also discussed. This study was further extended to spherical voids via 3D simulations [9]. In the work of Kapahi and Udaykumar [8], some grid refinement studies were shown. However, the converged solution did not indicate the formation of secondary heated regions as seen in the work of Bourne et al. [4]. The recent work by Levesque and Vitello [10] has shown the effect of various void shapes such as spherical, cylindrical, conical etc. on the post collapse temperature. It was observed that energy deposited by collapse of voids varies greatly with the shape of the voids. However, their work did not show the formation of secondary lobes for the spherical voids. The work of Kapila et al. [12] discussed the issue of grid convergence and sufficiently fine grids were used in the simulations. The use of finer grids allowed the capture of post-jetting secondary heated gas lobe regions. It is found that these secondary regions are important as reaction can initiate at these high temperature regions. This supports the observation of Bourne et al. [4], where secondary heated regions were shown to produce a brighter flash than the first flash (at the site of primary void collapse) which has important implications for initiation. Therefore, the relative importance of the primary collapse of a void and the secondary lobe collapse is an unsettled issue. This work will clarify the loading regimes in which primary and secondary void collapse dominate in determining initiation thresholds.

In past meso-scale studies, the effect of grid resolution on the prediction of reaction initiation has not been addressed adequately, save for the study by Kapila et al. [12]. Table I lists the grid resolutions used in selected previous studies [7,8,11,12] of void collapse. The use of various grid resolutions for the void collapse simulations raises questions on our understanding of void collapse physics derived from the meso-scale simulations. First, the uncertainty in prediction of maximum temperature achieved at the primary hot spot formed due to jet impact needs to be assessed. Another open question is the implication of the secondary hot spot regions at side lobes following the initial jet impact on initiation thresholds. Also, the importance of these secondary heated regions for triggering sustained reaction has been questioned by Bourne et al. [4]. High resolution simulations are necessary to clarify all of these unresolved issues, even in the context of voids of circular cross-section, not to mention voids of arbitrary shapes.

In this work, we address the following key questions in the context of void collapse simulations: what is the grid resolution required for accurate prediction of reaction initiation due to void collapse? What computed quantity of interest should be used to evaluate the grid convergence criterion, i.e. a spatially-averaged quantity such as total internal energy rise or local hot spot characteristics such as maximum temperature? What are the uncertainties in these quantities of interest due to numerical (i.e. grid) resolution limits? Can we provide guidelines on adequate grid resolution which will be valid in different loading regimes, i.e. low to high shock strengths? Is it feasible to use finer grids while simulating a real meso-structure containing field of voids; if not what are the limitations of meso-scale simulations in predicting sensitivity of a porous explosive? These insights are crucial in the understanding of implications of void collapse phenomena for reaction initiation and will help guide further meso-scale computational studies of initiation of HEs.

II. METHODS

A well-tested massively parallel Cartesian grid-based Eulerian solver SCIMITAR3D [13,15,19–21] is used to perform the reactive void collapse simulations. SCIMITAR3D uses a narrow-band level set [22] approach to track the material interfaces. All interfaces are treated in a sharp manner. The interfacial conditions, on free surfaces and material-material interfaces are applied using a modified ghost fluid method [23]. In the current work, void collapse simulations are performed in a material modeled with the properties of HMX. HMX constitutive and reactive modeling has been an active area of research. As pointed out in the work of Menikoff et al. [24], HMX material models can affect the sensitivity predictions from meso-scale simulations significantly. Therefore, for the current work, the HMX material models discussed in the work of Menikoff et al. [24] are implemented in SCIMITAR3D. A 3-step reaction model given by Tarver et al. [25] is implemented to perform reactive void collapse simulations. Verification and validation of the constitutive modeling, reactive modeling and numerical schemes used are shown in the results section. In the computations performed here the collapse of cylindrical voids are analyzed. Previous work has examined 2D axisymmetric [7,11] as well as 3D void collapse [9]. The 2D simulations here are motivated by the desire to compare the results with other works, including experiments by Swantek et al. [2] and Bourne et al. [4], numerical simulations of Menikoff [6] and extensive recent work using molecular dynamics [16,17]. It is also motivated by the goal of extending the current work to voids of arbitrary shape [15,26] and to fields of voids [8] where the axisymmetric assumption does not apply and where 3D simulations become prohibitive. In fact, in a companion paper [27] we examine the physics and numerical resolution requirements for elongated voids of various orientations in the same 2D framework as in the current paper. In addition, we discuss the implications of the relative sensitivities of the cylindrical and elongated voids with regard to pressed energetic materials [26]. The current 2D simulations, taken together with the elongated void study [27], reveal interesting and important insights into the effect of void shape and orientation on setting initiation thresholds.

III. FORMULATION

In the current Eulerian framework the governing equations are comprised of a set of hyperbolic conservation laws [28] corresponding to the conservation of mass, momentum and energy, as given below:

$$\frac{\partial \rho}{\partial t} + div\left(\rho \vec{V}\right) = 0 \tag{1}$$

$$\frac{\partial \rho \vec{V}}{\partial t} + div\left(\rho \vec{V} \otimes \vec{V} - \sigma\right) = 0 \tag{2}$$

$$\frac{\partial \rho E}{\partial t} + div\left(\rho E \vec{V} - \sigma \vec{V}\right) = 0 \tag{3}$$

where, $\vec{V}$ is velocity, ρ is density, E is the specific internal energy and σ is the Cauchy stress tensor. The stress state of material, σ can be decomposed into deviatoric part, S and dilatational part, P:

$$\sigma = S - PI \tag{4}$$

In the current Prandtl-Reuss formulation the deviatoric stress tensor S is given by the evolution equation in the rate form:

$$\frac{\partial \rho S}{\partial t} + div\left(\rho \vec{V} S\right) + \frac{2}{3}\rho G tr(D) I - 2\rho G D = 0 \tag{5}$$

where, D is strain rate tensor, and G is the shear modulus of material.

A. Constitutive model for HMX

The current work is aimed towards the computational modeling of porous HMX. The constitutive model for HMX used in the present framework follows closely the work of Menikoff et al. [24]. A brief description of the constitutive model is provided for the sake of completeness.

1. Equation of state

The hydrostatic pressure, P in Eq. (4) is obtained from the Mie-Gruneisen form of equation of state:

$$P = P_C(V) + \frac{\Gamma(V)}{V}\left[e - e_C(V)\right] \tag{6}$$

where, P_C corresponds to the isotherm for HMX. A Birch-Murnaghan form is used to represent the isothermal P-V relationship for HMX [29]:

$$P_C(V) = \frac{3}{2}K_0\left[(V/V_0)^{-7/3} - (V/V_0)^{-5/3}\right]\left[1 + \frac{3}{4}\left(K_0^{/} - 4\right)\left\{(V/V_0)^{-2/3} - 1\right\}\right] \tag{7}$$

and $e_C(V)$ is the internal energy on the isotherm:

$$e_C(V) = e_0 - \int_{V_0}^{V} P_C(V)\, dV \tag{8}$$

where, V is the specific volume, V_0 is the reference specific volume and e_0 is the reference energy corresponding to the room temperature $T_0 = 298\,K$. $\Gamma(V)$ is the Gruneisen coefficient. The equation of state constants mentioned in equation 7 are listed in Table II [29].

2. Specific heat

In the present framework, temperature is obtained from the calculated internal energy using the relationship [29]:

$$T(V, e) = T_0(V/V_0)^{\Gamma} + \frac{e - e_C(V)}{C_V} \tag{9}$$

where, C_V is the specific heat at constant volume. Specific heat varies with temperature as given by the relation,

$$C_V(\tilde{T}) = \frac{\tilde{T}^3}{c_0 + c_1\tilde{T} + c_2\tilde{T}^2 + c_3\tilde{T}^3} \tag{10}$$

where, $\tilde{T} = \frac{T}{\theta(V)}$ is a scaled temperature and $\theta(V)$ is the Debye temperature given by the expression,

$$\theta(V) = \theta_0 \left(\frac{V_0}{V}\right)^a exp[b\,(V_0 - V)/V] \tag{11}$$

The Gruneisen coefficient, $\Gamma(V)$ is obtained from the $\theta(V)$ as,

$$\Gamma(V) = -\frac{V}{\theta}\frac{d\theta}{dV} = a + b\frac{V}{V_0} \tag{12}$$

The values for the constants c_0, c_1, c_2, c_3, a and b are provided in Table II [29].

3. Strength model

The HMX material is assumed to exhibit viscoplastic behavior. The deviatoric part of the stress tensor, S (Eq. (4)) is modeled to capture this viscoplastic material response. The radial return algorithm for a viscoplastic material given by Ponthot [30] is used in the current framework. The radial return algorithm evolves the stress deviator, S as an elastic response first using a predictor step (Eq. (5)). Then the stress deviator is mapped back to the yield surface using a corrector step that enforces the viscoplastic flow rule. The values of yield stress, Y, shear modulus, G and the viscosity parameter η (to capture the viscoplastic behavior) used in the calculations are given in Table II [24].

4. Melt curve

Under high shock compression HMX can reach melting temperatures and loses its strength. The degradation of HMX strength under melting is modeled in the current framework using the Kraut-Kennedy expression of the melt curve of HMX given as,

$$T_m = T_{m0}\left(1 + a_1\frac{\Delta V}{V_0}\right) \tag{13}$$

where, constant a_1 can be estimated as $a_1 = 2\left(\Gamma - \frac{1}{3}\right)$. Therefore, as the temperature of the HMX reaches the melt temperature T_m, the deviatoric component of the stress tensor is set to zero.

B. Reactive modeling of HMX

The thermal decomposition of HMX is modeled using a multistep chemical kinetic model proposed by Tarver et al. [25]. Chemical decomposition of HMX takes place in 3 steps involving four different species. The three steps are given as,

<u>Reaction 1:</u> $HMX\ (C_4H_8N_8O_8) \rightarrow fragments\ (CH_2NNO_2)$

(14)

<u>Reaction 2:</u>

$$fragments\ (CH_2NNO_2) \rightarrow intermediate\ gases\ (CH_2O, N_2O, HCN, HNO_2) \tag{15}$$

Reaction 3:

$$2 \times intermediate\ gases\ (CH_2O, N_2O, HCN, HNO_2) \rightarrow \\ final\ gases\ (N_2, H_2O, CO_2, CO) \tag{16}$$

The rate equations for all the species are given as,

$$\dot{Y}_1 = -Y_1 Z_1 exp\left(-\frac{E_1}{RT}\right) \tag{17}$$

$$\dot{Y}_2 = Y_1 Z_1 exp\left(-\frac{E_1}{RT}\right) - Y_2 Z_2 exp\left(-\frac{E_2}{RT}\right) \tag{18}$$

$$\dot{Y}_3 = Y_2 Z_2 exp\left(-\frac{E_2}{RT}\right) - Y_3^2 Z_3 exp\left(-\frac{E_3}{RT}\right) \tag{19}$$

$$\dot{Y}_4 = Y_3^2 Z_3 exp\left(-\frac{E_3}{RT}\right) \tag{20}$$

where, Y_i is the mass fraction of the i^{th} species, Z_i is the frequency factor for each reaction, E_j is the activation energy for each reaction, R is the universal gas constant and T is the temperature. The values for each of these constants are provided in Table III [25]. The change in temperature because of the chemical decomposition of HMX is calculated by solving the evolution equation,

$$\rho C_p \dot{T} = \dot{Q}_R + \lambda \Delta T \tag{21}$$

where, ρ is the density of HMX, C_p is the specific heat of the reaction mixture, T is the temperature, λ is the thermal conductivity of the reaction mixture, Δ is the Laplacian operator and $\dot{Q}_R$ is the total heat release rate from all the reactions (Eq. (14)-(16)) and is given as,

$$\dot{Q}_R = \sum_{I=1}^{3} Q_I \dot{Y}_I \tag{22}$$

where, $I = 1 - 3$ is the reaction number (Eq. (14) – (16)), Q_I is the energy release from each of the reactions. The value for Q_I is tabulated in Table III.

The values of λ and C_P for the reaction mixture are obtained by weighted mass fraction average of the specific heat and thermal conductivity for the four species,

$$C_P = \sum_{i=1}^{4} C_P^i Y_i \tag{23}$$

$$\lambda = \sum_{i=1}^{4} \lambda_i Y_i \tag{24}$$

where, C_P^i and λ_i are the specific heat capacity and thermal conductivity for the four species obtained from the work of Tarver et al. [25]. The values for the C_P^i and λ_i for each of the species for various temperatures are listed in Table IV [25].

1. Numerical algorithm for the reactive system of equations

The governing equations along with the evolution of deviatoric stresses are spatially discretized using a 3rd-order essentially non-oscillatory scheme [31] and numerically integrated using 3rd-order Runge-Kutta scheme. To simulate the reactive mechanics of void collapse the HMX chemical kinetics model is coupled with the governing system of equations for mass, momentum, energy and evolution of deviatoric stresses. In the current Eulerian framework, the chemical species which are formed after decomposition of HMX are evolved in time by solving:

$$\frac{\partial \rho [Y_i]}{\partial t} + div\left(\rho \vec{V} [Y_i]\right) = \dot{Y}_i \tag{25}$$

where, $Y_i$is the mass fraction of the i^{th} species and $\dot{Y}_i$ is the production rate (equations (17-20)) source term for the i^{th} species.

At high temperatures the time scales of chemical reactions and species transport may differ by several orders of magnitude. Therefore, for higher temperatures several constraints must be applied on the time stepping of the governing equations apart from usual CFL-type stability criterion; such numerical stiffness may lead to very small time steps and infeasible flow calculations. This problem is circumvented by using a Strang operator splitting approach [32]. First, advection of species is performed using the flow time step to obtain predicted species values:

$$\frac{\partial \rho [Y_i]^*}{\partial t} + div\left(\rho \vec{V}^n [Y_i]^*\right) = 0 \tag{26}$$

In a second step, the evolution of the species mass fraction due to chemical reactions is calculated:

$$\frac{d[Y_i^{n+1}]}{dt} = \dot{Y}_i^n \tag{27}$$

The species evolution Eq. (26) is solved using the 5th-order Runge-Kutta Fehlberg [33] method, which uses an internal adaptive time-stepping scheme to deal with the stiffness of the chemical kinetic equations.

C. Interfacial Conditions

In the current work, the material interfaces are handled using the narrow-band level set approach [22]. The level set approach allows for tracking of the interfaces in a sharp manner and can handle large deformation of the materials as in the formation of material jets and collapse of the voids. Modeling of void collapse involves accurate treatment of the material-void interface. In the present work, the air in the void is not considered and the void is assumed to be vacuum. Therefore, zero stress conditions are implemented at the material-void interface and zero gradient conditions are imposed on the temperature and species concentrations. The necessary interfacial conditions are implemented using a modified ghost fluid method [23]. Detailed description of the numerical framework can be found in previous work [13,19,20].

D. Computational setup

High resolution simulations of the collapse of a cylindrical void are performed with three primary objectives: 1) to establish guidelines on the resolution requirements for meso-scale simulations of void collapse, 2) to resolve conflicting results in the literature on the value and location of the maximum temperature that occurs when the void collapses and 3) to identify the potential effect of primary and secondary void collapse on the initiation threshold in HMX. To study these aspects a single cylindrical void embedded in a homogeneous HMX matrix is considered in the current work. The computational domain is shown in Figure 2 and consists of a cylindrical void of $10\ \mu m$ diameter embedded in a square domain of size $45\ \mu m \times 45\ \mu m$. The shock loading is imposed as a particle velocity boundary condition from the west face of the domain; this mimics conditions encountered in flyer plate experiments on explosive samples. The shock load is applied for $3\ ns$. The east, north and south faces of the computational domain are supplied with the outlet boundary condition. In all the simulations involved in the current study, the computational set up remains the same and only the imposed velocity magnitude is varied to impose loads of different strengths.

IV. RESULTS

The uncertainty associated with the grid resolution in predicting initiation in porous HMX is studied using meso-scale void collapse simulations. The effect of grid resolution on the sensitivity of HMX is analyzed under various shock strengths. The results obtained from the current analysis are categorized and presented in the following sections; in section IV.A, the mechanical response and reactive models for HMX are verified. The numerical framework for void collapse simulations is validated and verified against the past experimental and computational results; section IV.B presents the grid convergence study for a single cylindrical void under $500\ m/s$ and $1000\ m/s$ shock strengths. The grid refinement criterion for $500\ m/s$ and $1000\ m/s$ is compared; section IV.C analyzes the reasons for the discrepancy in the refinement criterion for low ($500\,m/s$) and high ($1000\,m/s$) shock strengths. All the aforementioned grid convergence studies pertain to inert meso-scale simulations; section IV.D and section IV.E then compares and contrasts the reactive void collapse simulation results for the low ($500\,m/s$), high ($100\,m/s$) and very high ($2000\,m/s$) shock strengths to examine the uncertainty associated with the grid resolution in reaction initiation for different shock strengths.

A. Verification and validation

1. Verification of implementation of the material and reactive models for HMX

In this section, the equation of state (isotherm and Hugoniot) and the specific heat capacity variation with temperature are compared with the results of Menikoff et al. [29]. The isotherm and Hugoniot for HMX is calculated for various compression ratio from Eq. (6) and Eq. (7). The isotherm and Hugoniot matches closely with Menikoff et al. [29] results (Figure 3(a)). The temperature variation of the specific heat also matches with Menikoff et al. [29] calculations (Figure 3(b)).

Having verified the constitutive models for HMX, the next step is to verify the reactive model for HMX decomposition. The 3-step chemical kinetic model of Tarver et al. [25] for HMX decomposition is used in the current analysis (section III.B). In the work of Tarver et al. [25], the 3-equation reaction kinetics for HMX was used to obtain a threshold curve for HMX initiation. The threshold curve was obtained by performing reaction-diffusion calculations in a uniform HMX material containing a hot spot. The calculations were performed by instantaneously heating a hot spot of a certain shape (cylindrical, spherical or planar) at a specified temperature. The HMX surrounding the hot spot was kept at room temperature (293K). The reaction-diffusion calculations were performed to investigate whether the imposed hot spot of specified size and temperature leads to ignition or whether the hot-spot dies off. Tarver et al. [25] provide a threshold curve for different hot spots shapes i.e. cylindrical, spherical and planar. Because this work is primarily focused on cylindrical voids, the critical hot spot curve is obtained for cylindrical hot spots. For verification, the current work obtains this critical hot spot curve using the reaction kinetics implementation. To this end, the reaction diffusion calculations to compute the evolution of a cylindrical hot spot are performed by solving Eq. (21). Figure 4(a) shows the numerical set up for the present calculations. Zero gradient temperature boundary condition is imposed on all the domain boundaries. The hot spot sizes and shapes are varied to find the critical point beyond which reaction will be imminent. The criterion for the critical hot spot is obtained by repeating these calculations for different hot spot sizes. The threshold curve is in good agreement with the Tarver et al. [25] result for prediction of the critical condition (Figure 4(b)). This verifies the parts of the implementation that pertain to chemical kinetics modeling and diffusive transport.

2. Validation of the numerical solver for hydrodynamic void collapse

Swantek et al. [2] performed void collapse experiments by loading a gel composed of agarose and glycerol containing cylindrical voids of $3\,mm$ diameter. The loading was applied using a gas gun projectile impacting an aluminum striker. The focus of the experiments was to understand the hydrodynamics of void collapse. The results of Swantek et al. [2] are used for the validation of the numerical framework in predicting the dynamics of collapse of voids. In previous work [8], comparison of the cylindrical void collapse simulation with the results of Swantek et al. [2] was performed. However, the constitutive model for HMX used previously was different from the current implementation. Therefore, the comparison with the experimental result is repeated in the current work with the updated models.

The computational set up shown in Figure 2 is used to perform the void collapse simulation. A shock velocity of $V = 500\, m/s$ is imposed on the west face of the domain boundary. A grid size of 0.01 μm is used. This translates to 100 grid points across the diameter of the cylinder. Figure 5 shows the evolution of the normalized diameter of the collapsing void with respect to the normalized time. The normalized diameter is defined as the ratio of the centerline length of the deformed void to the original diameter. The normalized time is defined as:

$$\tau = \frac{t_c - t_o}{t_f - t_o} \tag{28}$$

where, $t_o$is the time when void starts to deform, t_c is the current time as void is deforming and t_f is the final collapse time recorded when the upstream surface of the void impacts the downstream surface along the centerline diameter.

Figure 5 shows that the result from the current analysis, for the variation of the normalized void diameter plotted against normalized time, is in good agreement with the experimental result of Swantek et al. [2]. This validates the current solver for void dynamics up to collapse in the inert case.

3. Verification of inert void collapse simulations for HMX

The previous section shows that the collapse profile of the cylindrical void in HMX matches the experimental results of Swantek et al. [2]. However, the shock profile and the void collapse temperature cannot be compared with the experiments of Swantek et al. [2] because the material used in the experiments is not HMX. There are no experimental data available to validate the meso-scale simulations involving void collapse in HMX. Therefore, past [6,34] meso-scale simulations are used to verify the accuracy of the numerical framework for the prediction of shock dynamics and the void collapse temperature.

Menikoff [6] performed an inert void collapse simulation in HMX which can be used as a potential benchmark. Figure 6(a) shows the numerical setup used in the analysis of Menikoff [6]. A cylindrical void of radius $0.1\, mm$ in HMX domain of size $1\, mm \times 0.5\, mm$ is subjected to a shock, driven by a piston moving with a speed of $1.3\, km/s$. The piston load is applied from the west face of the domain boundary. The void is resolved with 300 grid points across the diameter. Figure 6(b) shows the temperature contours after the collapse of the void. The shock profile obtained from the current analysis (contours in Figure 6(b)) is compared with the results (black dots) of Menikoff's [6] analysis (Figure 6(b)). The location of the leading shock, secondary shock, contact discontinuity and Mach stem match closely with Menikoff's [6] results. The Mach triple point is observed to be located at $(0.825\,mm,\ 0.14\,mm)$ which closely matches the location from Menikoff's [6] simulation ($(0.82\,mm,\ 0.14\,mm)$).

The current numerical framework is further verified with the results of Springer et al. [34]. Springer et al. [34] performed void collapse simulations in HMX for a spherical void. The spherical void was modeled using 2D axisymmetric analysis. A void of $1\ \mu m$ diameter was analyzed under the shock loading of $25\,GPa$. In the current setting, a cylindrical void of diameter $1\ \mu m$ is analyzed under the same loading condition of $25\,GPa$ pressure. Table V compares the results obtained from the current simulations with the results of Springer et al. [34]. The bulk temperature rise from shock heating, jet impact speed and the temperature reached after the collapse of the void are compared. The results are in good agreement with those of Springer et al. [34].

B. Grid convergence study

Grid resolution plays a crucial role in shock induced void collapse simulations. Previous void collapse analyses [7,8,10,11] have not established a grid refinement criterion that is applicable for various loading regimes. In this work, grid convergence studies are performed to establish grid refinement criterion for the collapse of a cylindrical void under low ($500\ m/s$) and high ($1000\ m/s$) shock strength. The studies are performed for inert HMX i.e. by switching off the chemical reaction.

1. Grid convergence study for $500\ m/s$ *shock load*

This section establishes the grid refinement criterion for low ($500\ m/s$) shock strength. Figure 2 shows the computational setup used in the current analysis. A particle velocity of $500\ m/s$ is applied to the west face of the domain boundary (Figure 2). Four different grid sizes are considered: $0.1\ \mu m$, $0.03\ \mu m$, $0.02\ \mu m$ and $0.014\ \mu m$. The grid sizes correspond to 100, $300, 500$ and 700 grid points across the void diameter ($= 10\ \mu m$).

For shock induced void collapse a grid refinement criterion should be established based on the hot spot intensity. The hot spot intensity can be quantified using global and local measures. A global measure such as total specific internal energy (Eq. (29)) quantifies the net energy deposited in HMX following the void collapse. On the other hand, local measures such as the maximum temperature following collapse provides detailed information about the impact of the collapse event on temperature rise and the reaction initiation at the hot spot. This study establishes grid refinement criterion with respect to both global and local measures.

$$\text{Total specific internal energy, } e_T = \frac{\int_V \rho e\, dV}{\int_V \rho\, dV} \tag{29}$$

where, e_T is the total specific internal energy in the sample, ρ is the density and e is the computed specific internal energy field.

Figure 7(a) compares the time variation of the total specific internal energy for the four grids. Total specific internal energy increases with time for all the grids. This increase is because of the energy deposition following the collapse of the void under shock load. Grid resolution corresponding to 100 grid points across the cylinder diameter is sufficient to obtain a converged solution for the energy deposition (Figure 7(a)). Figure 7(b) shows the time evolution of the maximum temperature in the domain for the four grids. The maximum temperature in the domain increases with refinement. The variation of the maximum temperature for the different grid sizes is highest near the intermittent peaks observed in the temperature-time trends (Figure 7(b)). It is noted that for the convergence of maximum temperature, 500 grid points across the cylinder diameter are required. The grid refinement criterion for convergence of the maximum temperature is observed to be more stringent when compared to that for the total specific internal energy. This is because total specific internal energy is an average estimator of the hot spot intensity and smears out the local behavior of the hot spots. Therefore, global measures can be unduly forgiving and can lead to an underestimation of the required grid resolution. Local measures such as maximum hot spot temperature are more reliable indicators of convergence with respect to grid refinement. The hot spot local temperatures are important to capture accurately because they can affect the prediction of initiation of chemical reactions through Arrhenius-type rate equations in the Tarver 3-equation model [25]. Therefore, 500 grid points across the void diameter are necessary to obtain converged results of hot spot intensity for low shock strength ($500\ m/s$) loading.

2. Grid convergence study for $\mathbf{1000}\ \boldsymbol{m/s}$ *shock load*

The above analysis with $500\ m/s$ shock strength indicates that the grid resolution that accurately captures the local measure (such as maximum temperature) of a hot spot should be used for reliable void collapse simulations. The local behavior of a hot spot is dependent on the void morphology and the shock strength. The effect of void morphology on grid convergence is analyzed in a companion paper [27]. Here the effect of shock strength on the grid refinement criterion is studied for a void of $10\ \mu m$ diameter (Figure 2). A shock of strength corresponding to $1000\ m/s$ particle velocity is applied from the west face of the boundary. Five different grid sizes are considered: $0.1\ \mu m$, $0.03\ \mu m$, $0.02\ \mu m$, $0.014\ \mu m$ and $0.01\ \mu m$. These grid sizes correspond to 100, 300, 500, 700 and 1000 grid points across the void diameter ($= 10\ \mu m$).

The maximum temperature in the domain is used for establishing the grid refinement criterion (Figure 8(a)). The maximum temperature in the domain increases with grid refinement. This trend is more pronounced in the time range where the maximum temperature peaks are observed (Figure 8(a)), i.e. between $5.2\ ns - 6\ ns$. To gain insight into the convergence behavior of the maximum temperature peaks, the maximum temperature plot of Figure 8(a) is magnified in Figure 8(b) for the time duration of $5.2\ ns - 6\ ns$. Figure 8(b) shows the rise in the maximum temperature peaks occurs in two phases. The first phase corresponds to the initial peak of maximum temperature of value $1500\ K$ at time $5.25\ ns$, which is the primary peak. Following the primary peak, there are a series of secondary maximum temperature peaks observed (Figure 8(b)). The magnitudes of secondary peaks are higher than the primary peak (Figure 8(b)). The grid convergence requirement for the primary and secondary peaks vary from each other. The primary peak values converge to $1500\ K$ for a grid corresponding to 500 points across the void diameter. Secondary peaks do show a convergent trend with grid refinement. However, the peaks do not show complete convergence even for the finest grid used in the analysis i.e. 1000 grid points across the void diameter. The grid convergence study for this high strength shock indicates that secondary peaks are grid dependent even for the finest grid used in the computations. However, a sufficiently fine grid is required to be used in meso-scale simulations of shocked porous materials because coarse grids can significantly under-predict the maximum temperature (Figure 8(b)). For instance, the difference between the secondary peak values in the maximum temperature plot for the coarsest grid (i.e. 100 points) and the finest grid (i.e. 1000 points) is roughly $1900\,K$ (Figure 8(b)). On the other hand, this difference for two consecutive refined grids i.e. 700 and 1000 points is around $400\,K$. Therefore, for feasible meso-scale simulations that can still capture secondary void collapse and corresponding peak temperatures, 700 points across the cylinder diameter need to be used for simulations of void collapse for higher shock strengths ($1000\,m/s$ and above).

3. Comparison of grid requirements for low and high shock strength

In section IV.B.1 and IV.B.2, the grid resolution requirements are shown to be strongly dependent on the shock strength. For low shock strength ($500\,m/s$), the formation of a single maximum temperature peak is observed. This maximum temperature peak converges for 500 points across the cylinder diameter. For high shock strength ($1000\,m/s$), the maximum temperature rise is observed in two phases. The primary peak converges for 500 grid points across the void diameter; while secondary peaks do not converge for the grid resolutions used. Therefore, it is the emergence of secondary peaks at high shock strengths that poses challenges to obtaining a grid independent solution for void collapse induced hot spots. Previously reported void collapse simulations [6–8,11] were performed for various shock strengths and grid resolutions. In some cases coarse grids corresponding to 100 points across the void diameter were used even for the higher strength shock loading (Table I). In light of current analysis most previously reported void collapse simulations [6–8,11] were not adequately resolved to capture the dynamics of secondary voids.

C. Primary and secondary temperature peaks

It is clear that grid resolution introduces uncertainty in the prediction of hot spot temperatures in meso-scale simulations. This is because the magnitudes of the primary and secondary peaks are strongly dependent on grid sizes. A deeper understanding of the primary and secondary peak dependencies on grid resolution can be gained by distinguishing the physical mechanisms governing the formation of these peaks. To this end, the following questions are posed: What are the physical mechanisms responsible for the formation of primary and secondary peaks in local temperatures? Why is the secondary peak temperature higher than the primary peak? Why is the grid convergence criterion for secondary peaks more stringent than the primary peak, especially for high shock strength loading conditions? These questions are answered in the following section by analyzing the collapse of the void in the setup shown in Figure 2.

1. Physical mechanisms corresponding to the formation of primary and secondary peaks

The collapse of the void shown in Figure 2 is analyzed for the high shock load, with $1000\,m/s$ particle velocity. Figure 9 shows the time evolution of void collapse for a grid resolution of 700 points across the void diameter. The numerical Schlieren and temperature contours are shown to obtain a deeper view of the collapse process. There are mainly five different stages in the collapse of the void for the shock strength of $1000\,m/s$. The first stage is the shock heating of the bulk HMX material which leads to a rather modest temperature increase. In the second stage, the shock wave starts to deform and accelerate the upstream surface of the void (Figure 9(i)). The third stage corresponds to the plastic dissipation in the material that forms the deformed rear surface of the void during the formation of a material jet (Figure 9(ii)). In the fourth stage, the material jet formed further strengthens and impacts the downstream surface of the void; this generates a primary blast wave that emanates from the point of impact (Figure 9(iii)). The velocity of the jet in this case is around $4.5\,km/s$, i.e. about 4 times stronger [34] than the imposed $1000\,m/s$ planar loading velocity. The primary blast wave is evident in the Schlieren and temperature contour plots (Figure 9(iii)). This jet impact causes the initial rise in temperature that is realized as the primary peak in the maximum temperature plot of $1000\,m/s$ shock load (Figure 8(b)). In the final i.e. fifth stage, the complete closure of the void takes place (Figure 9(iv)). After the initial jet impact, symmetrically placed secondary lobes are formed; these are fragments of the initial void. These secondary lobes are compressed under the combined influence of the incident shock load and the high strength primary blast wave that was formed during the initial jet impact. The secondary maximum temperature peaks in Figure 8(b) correspond to the closure of these secondary lobes.

2. Reasons for secondary peak temperatures being higher than the primary peak

The grid convergence study for the $1000\,m/s$ shock indicates that the secondary temperature peaks are higher than the primary peak (Figure 8(b)). The impact of the material jet from the upstream surface of the void on its downstream surface leads to the primary peak (Figure 9(iii)) or first flash [4]. The high kinetic energy of the jet is converted to the rise in internal energy once the jet impact occurs. Jet impact leads to the formation of secondary lobes and a primary blast wave (Figure 9(ii)). The collapse of the secondary lobes under the combined influence of the primary blast wave and incident shock load leads to the secondary temperature peaks. The plots of magnitude of the total velocity and total specific internal energy are used to analyze the collapse of the secondary lobes (Figure 10). There are two mechanisms that occur simultaneously during the closure of the secondary lobes; the acceleration of the secondary lobes causes the rise in the local kinetic energy (Figure 10(e)) and the pinching of the secondary lobes near the lobe tip (Figure 10(f)). The pinching action leads to a series of collapses of the secondary lobes and the generation of high strength secondary blast waves that strengthen the primary blast wave. The strengthening of the blast wave accelerates the void surface further, with further local increase in the kinetic energy. Each pinching instance causes conversion of the local kinetic energy into internal energy leading to the observed successive secondary peaks in temperature in Figure 8(b). This continues until the void completely collapses. Therefore, the successive collapse of the voids and strengthening of the blast wave through the pinching mechanism is the main cause for the secondary peak temperature to be higher than the primary temperature peak.

The self-strengthening of the blast waves because of pinching action creates high compression regions locally near the secondary lobe surface. The combined effects of high pressure and density gradients across the secondary lobe leads to the creation of barotropic vortices and intensely rotational velocity fields. Figure 11 shows the contour plots of the vorticity generated during the secondary lobe closure. The local rise in kinetic energy can also be related to the formation of material jets at the secondary lobe surface (Figure 10(e) and Figure 11(c)). As can be seen from the velocity field shown in Figure 10(e) and Figure 11(c), these material jets point towards each other because of the rotational velocity field. This leads to the collision of multiple opposed high velocity jets during the final closure event of the secondary lobes. Jet collision events are associated with very high temperature rises during secondary void collapse. The effective jet impact speed during the final closure at the secondary void was observed to reach a value of $6.5\ m/s$ which is higher than the initial jet impact speed of $4.5\ m/s$ at the primary void collapse site. It is interesting to note that the location of the jet collision coincides with high vorticity concentration regions. Therefore, regions of high vorticity accompany regions of maximum temperature rise and coincide with sites of reaction initiation.

Note that Bourne et al. [4] experiments indicated the formation of two symmetrical gas lobes from the collapse of the original void; they also observed that the secondary flash resulting from the collapse of the secondary lobes was brighter than the primary flash generated from the jet impact. In the present work the void is modeled as vacuum and the void surface is treated with free surface conditions. Therefore, the relevance of the observations regarding the secondary void collapse must take into account the limitations of the current model with respect to treatment of gas in the pore. The severe compression experienced at the site of the secondary collapse that leads to the elevated collapse temperature in the current work may also lead to compression of the gas in the pore. The resulting elevation of the gas to a higher adiabat may lead to the bright flash observed by Bourne et al. [4] in their experiments. It must be noted that molecular dynamics (MD) simulations by Eason and Sewell [16] also indicate high compression at the secondary lobe collapse locations and resulting high temperatures for strong shock induced collapse. In addition the secondary collapse regions are shown to be accompanied by high vorticity values. Although these simulations were performed for pores in the nanometer size range, the overall behavior of primary jet formation and secondary void compression and rotational flows is very similar to those observed in the current work.

3. Grid convergence of the secondary peaks

Secondary peaks can affect the sensitivity of the energetic material. The secondary maximum temperature peaks are found to be grid dependent and the peak value increases with refinement. The reason behind this discrepancy in the convergence behavior of the primary and secondary temperature peaks is of significance as it is related to the uncertainty associated with the grid resolution in predicting initiation in porous energetic materials. This section explains this discrepancy from the results obtained from the collapse analysis of the cylindrical void (Figure 2) under the shock load of $1000\ m/s$.

The convergence of the temperature peaks is dependent on the resolution of the void surface. Jet impact on the downstream surface of the cylindrical void governs the formation of the primary temperature peak. The jet impact event is dependent on the resolution of the initial cylindrical void. With grid refinement the cylindrical void becomes well resolved and the convergence of the primary maximum temperature peak is achieved. Therefore, the primary peak in temperature can be robustly predicted with sufficiently well resolved grids. However, the convergence of the secondary peak is dependent on the resolution of the secondary lobes. Poorly resolved secondary lobes affect their shapes obtained after the jet impact. To estimate the effect of grid resolution on the prediction of shape of the secondary lobes, the shape of one of the lobes just after the initial jet impact is compared for two grid sizes in Figure 12. The grid sizes correspond to 100 and 700 points across the initial void diameter. The shapes of the secondary lobe predicted by the coarse (Figure 12(a)) and fine grids (Figure 12(d)) vary significantly. The secondary lobe is under-resolved for the coarse grid (Figure 12(b)) and the shape of the lobe is narrower and smaller when compared to the fine grid case (Figure 12(e)). The tip of the secondary lobe is also under-resolved for the coarse grid (Figure 12(c)). The under-prediction of the size of the secondary lobe causes the pinching action to be less effective and leads to under-estimation of the secondary peak temperature. With refinement the shape of the secondary lobe is preserved leading to efficient pinching action and increase in the collapse temperature. Therefore, the grid convergence criterion for secondary peaks is dictated by the resolution of these secondary lobes and not the resolution of the original cylindrical void. The secondary lobes are generated during the course of shock propagation. In fact, the secondary lobe shapes are highly grid dependent, even for fine grids. This makes it difficult to develop a grid criterion that is applicable for the collapse of the cylindrical voids over various shock loading situations.

D. Importance of grid resolution on reaction initiation

The primary and the secondary temperature peaks can have significant influence on the shock initiation of porous energetic materials. Therefore, it is important to understand the impact of the accurate prediction of these peaks on the prediction of ignition. This section is aimed towards analyzing the importance of the aforementioned primary and the secondary peaks on ignition in different loading regimes. Three different shock strengths are considered amounting to imposed particle velocities of $500\,m/s$, $1000\,m/s$ and $2000\,m/s$. The computational set up is shown in Figure 2; a cylindrical void of diameter $10\,\mu m$ is used for the analysis. The grid resolution for $500\,m/s$ shock load corresponds to 500 grid points across the cylinder diameter. 700 grid points across the cylinder diameter are used for the other two shock strengths. In this section, reactive voids collapse simulations are performed using the Tarver 3-equation HMX model [25] (section III.B). The reaction completion for the Tarver 3-equation model is identified by observing the mass fraction of the final gaseous species (Eq. (16)). The value of 0 corresponds to no reaction and 1 corresponds to complete reaction. The results of the three simulations are discussed in the following sections.

1. Reactive void collapse under $500\,m/s$ *shock load*

The reactive void collapse simulation under the shock load of $500\,m/s$ is shown in Figure 13. The temperature and the mass fraction of the final gaseous species are shown for four different instants during the course of void collapse. The simulation is carried out to diffusion time scales (order of microseconds). The collapse of the void leads to the initial jet impact forming the primary temperature peak. However, the maximum temperature reached is not sufficient to initiate reaction. In this case the hot spot formed is eventually quenched as thermal diffusion redistributes the hot spot energy to the surrounding material. There are no gaseous species production observed (Figure 13(b)). In this case the use of an under-resolved grid will under-predict the hot spot temperature but will not affect the initiation of chemical reactions due to the relatively low imposed shock strength. This loading condition where the hot spot is formed but eventually diffuses away can be categorized as a “sub-critical” loading condition.

2. Reactive void collapse under $1000\ m/s$ *shock load*

It was shown earlier that for void collapse under high strength shock i.e.$1000\ m/s$ the second peak temperature is very high. Also, the second peak temperature is under-predicted for simulations performed on coarser grids. Figure 14 shows the temperature and mass fraction of final gaseous species contours. Figure 14(c, d) shows that jet impact causes the formation of the primary temperature peak. However, the primary temperature peak is not sufficient to ignite the HMX material. The initial jet impact forms the primary blast wave and two symmetrical secondary lobes. The collapse of these secondary voids causes the formation of secondary peaks (Figure 14(e)). The secondary peak temperature is high enough to cause ignition at the secondary lobe locations (Figure 14(f)). As the collapse of the secondary lobes progresses, further rise in temperature takes place which is also augmented by energy released because of chemical reactions. Eventually, the complete collapse of the secondary lobes takes place and ignites the HMX material at the secondary lobe locations. For this $1000\ m/s$ shock, the initial jet impact is not sufficient to initiate reaction. Instead, reaction initiates at the offset locations where secondary lobes are collapsed. Using a coarser grid may predict the primary blast wave accurately, but the secondary lobes will be under-resolved leading to failure to initiate sustained reactions. Therefore, the use of highly refined grid is required under the high strength shock loading situations as with the $1000\ m/s$ shock. This loading condition where the secondary peaks are responsible for ignition can be categorized as “critical”. Note that it is the secondary void collapse that first leads to the critical condition for initiating reactions in the material.

3. Reactive void collapse under $2000\ m/s$ *shock load*

For $2000\ m/s$ shock, the initial jet impact (Figure 15(c)) is very strong and causes the formation of the primary temperature peak which is sufficient to ignite HMX (Figure 15(d)) at the primary jet impact location. The secondary lobes created from the initial jet impact further collapse under the influence of the primary blast wave (Figure 15(e)). The reaction initiated near the primary jet impact location spreads further as the secondary lobes collapses at a higher temperature. The chemical reaction energy release therefore strengthens because of the collapse of the secondary lobes. As pointed out earlier, the primary temperature peaks are accurately predicted even with a relatively coarse grid. Therefore, for extreme loading situations where primary peaks are sufficient to initiate reactions the use of coarser grids may not affect the prediction of ignition. The uncertainty in the prediction of ignition with respect to the grid resolution is therefore lower under extreme loads. This loading condition where the primary peak is responsible for reaction initiation can be categorized as “super-critical”.

E. Uncertainty associated with grid resolution

The use of highly refined grids for predicting initiation of porous energetic materials may pose challenges for meso-scale simulations of "real" microstructures where a field of voids is present. In this work, we have shown that there is significant amount of uncertainty that can arise from less than adequate grid resolution for predicting reaction initiation, even for a single void. Resolving each void adequately in a real microstructure will increase the computational costs significantly to the point of making accurate meso-scale calculations infeasible. Therefore it is important to assess the implications of the present grid resolution studies for simulations involving fields of voids.

It was shown in the previous section that resolution-induced uncertainty in threshold prediction is a function of loading conditions. The threshold for the "critical" loading condition i.e. $1000\,m/s$ is prone to greater uncertainty than for the "sub-critical" ($500\,m/s$) and "super-critical" $2000\,m/s$ cases. The main reason for this dependency is the relative importance of primary and secondary temperature peaks -- grid resolution has greater relevance for situations where secondary temperature peaks can initiate chemical reactions. For loading conditions where reaction will not initiate at all i.e. sub-critical conditions, or where the primary collapse temperature peaks are responsible for the reaction initiation i.e. super-critical conditions, grid resolution may not carry serious implications for prediction of thresholds.

To understand the relative importance of primary and secondary peaks, the convergence of maximum primary and maximum secondary temperatures for the above three shock loads is shown in Figure 16. For $500\,m/s$ shock the primary and the secondary peak temperatures are equal. There are two important observations from Figure 16. First, the primary temperature peak is accurately predicted even for the coarsest grid i.e. corresponding to 100 grid points across the void diameter. This is the level of resolution employed in some previous works on void collapse[6–8,11] (Table I). Second, the discrepancies between primary and the secondary peak temperature increases with the increase in shock strength. Therefore, for sub-critical loads resolving the void with the coarsest grid will not change predicted ignition conditions. Similarly, for the super-critical loading condition, as the primary temperature peak is fairly accurately predicted even with the coarsest (100 points across D) grid, the use of such grid resolutions may not change sensitivity predictions. However, the problem lies in the critical loading situations where the secondary peak is more important for ignition prediction; the use of coarse grids will not result in correct ignition predictions. For critical loading situations, finer grids, up to 700 grid points across the void diameter may be required for accurate ignition predictions. Note that, as observed by Bourne et al. [4] the hot spot sizes caused by the secondary void collapse are indeed smaller than those produced by the primary void collapse. However, the temperatures at such collapse points are considerably higher (see Figure 14(e)) than at primary void collapse points. Whether such smaller, more intense hot spots will lead to initiation more effectively than larger, lower temperature hot spots, particularly in complicated meso-structures involving void fields, remains to be assessed. A starting point for such analysis is provided by the so-called Tarver critical hot spot curve [25]. The critical hot spot curve indeed indicates that smaller, high temperature hot spots can cause initiation while larger hot spots at lower temperatures can achieve criticality. The present simulations show that whether primary or secondary void collapse lead to critical hot spots depends on the imposed load and other characteristics of voids, including void-void interactions [8]. In a companion work [27] we show that the matter of critical hot spots can become further complicated by aspects of void shape (aspect ratio) and void orientation.

V. CONCLUSIONS

This work addresses a key unsettled question: what is an “adequate” grid resolution required to perform reactive void collapse simulations for accurate prediction of ignition from hot spots? A Cartesian grid based Eulerian solver SCIMITAR3D is used to study the problem of void collapse in HMX. The HMX reactive modeling is performed using the Tarver 3-equation reaction mechanism. The numerical framework and the implementation of the constitutive model for HMX is verified and validated against benchmark numerical and experimental results.

Determining convergence of void collapse calculations by relying on spatially averaged quantities such as total specific internal energy can be misleading for void collapse because the reaction initiation is based on local features such as hot spot temperature. Therefore, for this category of problems it is required to develop grid convergence criteria based on local hot spot features such as maximum temperature in the hot spot. The required grid resolution turns out to be a function of imposed shock loading conditions. For low shock loading, in the present work the $500\,m/s$ shock, the converged solution can be obtained with 500 grid points across the cylinder diameter. However, for intermediate strength shock strengths i.e.$1000\,m/s$, $700-800$ grid points are required. Interestingly, for very high shock loading, i.e. 2000 m/s, the grid resolution requirements again become lower, i.e. it is possible to use $300-500$ points (or even fewer, say 100 points) across the void. The reason for this dependency is because the void collapse shapes and trajectories vary significantly depending on the loading conditions. For lower shock strength, the material jet shape is such that secondary lobes are not formed. Therefore, only a primary peak temperature results due to collapse of the original void. However, as the size of the secondary lobes are bigger for higher shock loads, collapse of secondary lobes leads to high temperatures that can initiate reactions. The grid resolution required to capture the dynamics of secondary lobes is significantly higher. Therefore highly resolved simulations are required for high shock strength loading situations. It is observed that after the initial jet impact, the velocity field is highly rotational near the secondary lobes. There is intense generation of barotropic vortices after the initial jet impact; this arises due to the interaction of the blast wave emanating from the point of first collapse with density gradients in the vicinity of the collapsing secondary lobes. The high secondary peak temperature co-locate with regions of maximum vorticity, i.e. in the core of the vortices. These phenomena have also been observed in MD simulations [16] of the collapse of nanoscale voids. In particular, strong compression at secondary lobes offset from void centerlines and accompanying strong vorticity concentrations are exhibited by MD simulations as well. The pinching of secondary voids leading to high temperature hot spots is also seen to be well aligned with MD simulations.

The current work treats the void material as vacuum. Therefore, the observations made regarding the secondary void collapse and its influence on the grid convergence must take into account the limitations of the present framework with respect to treatment of gas in the void. The severe compression experienced at the secondary void collapse locations that leads to the elevated collapse temperature may also lead to compression of the gas in the void. This severe compression of void may result in the elevation of the gas to a higher adiabat as observed by Bourne et al. [4] in their experiments through a bright flash.

This work also investigated the effect of loading strength on reactive void collapse using high resolution simulations. In the sub-critical ($500\,m/s$) loading regime the collapse of the voids form hot spots that diffuse out and no reaction is observed. In the critical loading regime ($1000\,m/s$) secondary lobe collapse is responsible for initiation of chemical reaction and ignition. In the super-critical loading regime ($2000\,m/s$) the primary void collapse itself causes a strong enough temperature rise to cause ignition. It is observed that the grid resolution-related uncertainty in predicting ignition is higher in the critical loading regime when compared to the sub- and super- critical loading regimes. This observation has implications for meso-scale simulations involving real microstructures where resolving each of the voids to the finest level required is practically infeasible. In such meso-scale simulations, particularly in intermediate loading regimes under-resolution of voids can lead to incorrect predictions of the initiation threshold. The rather stringent resolution requirements for void collapse simulations indicate that adaptive grid resolution, for example through AMR [35] (adaptive mesh refinement) or LMR [19] (local mesh refinement) will prove useful.

The present work indicates that whether primary or secondary void collapse lead to critical hot spots depends on the imposed load. However, other characteristics of voids, including void-void interactions [8] and three-dimensional effects [9] have not been assessed in this work. Additionally, in a companion work [27] it is shown that the issue of hot spot formation and meso-scale simulations of such phenomena can become further complicated by aspects of void shape (aspect ratio) and void orientation. All of these additional effects remain to be investigated to obtain a comprehensive understanding of void collapse induced hot spot formation in porous energetic materials.

VI. ACKNOWLEDGEMENT

This work was performed under grants from the AFOSR Computational Mathematics program (Program Manager: Dr. Jean-Luc Cambier) and from the AFRL-RWPC (Computational Mechanics Branch, Eglin AFB)).

[1] Field, J. E., 1992, “Hot Spot Ignition Mechanisms for Explosives,” Acc. Chem. Res., **25**(11), pp. 489–496.

[2] Swantek, A. B., and Austin, J. M., 2010, “Collapse of Void Arrays under Stress Wave Loading,” Journal of Fluid Mechanics, **649**, pp. 399–427.

[3] Bourne, N. K., and Field, J. E., 1991, “Bubble Collapse and the Initiation of Explosion,” Proceedings of the Royal Society of London A: Mathematical, Physical and Engineering Sciences, **435**(1894), pp. 423–435.

[4] Bourne, N. K., and Milne, A. M., 2003, “The Temperature of a Shock-Collapsed Cavity,” Proceedings of the Royal Society of London A: Mathematical, Physical and Engineering Sciences, **459**(2036), pp. 1851–1861.

[5] Baytos, J. F., Craig, B. G., Campbell, A. W., Deal, W. E., Dick, J. J., Dinegar, R. H., Engelke, R. P., Larson, T. E., Marshall, E., and Ramsay, J. B., 1980, *LASL Explosive Property Data*, Univ. of California Press, Berkeley.

[6] Menikoff, R., 2004, “Pore Collapse and Hot Spots in HMX,” *AIP Conference Proceedings*, IOP INSTITUTE OF PHYSICS PUBLISHING LTD, pp. 393–396.

[7] Tran, L., and Udaykumar, H. S., 2006, “Simulation of Void Collapse in an Energetic Material, Part I: Inert Case,” Journal of propulsion and power, **22**(5), pp. 947–958.

[8] Kapahi, A., and Udaykumar, H. S., 2013, “Dynamics of Void Collapse in Shocked Energetic Materials: Physics of Void–void Interactions,” Shock Waves, **23**(6), pp. 537–558.

[9] Kapahi, A., and Udaykumar, H. S., 2015, “Three-Dimensional Simulations of Dynamics of Void Collapse in Energetic Materials,” Shock Waves, **25**(2), pp. 177–187.

[10] Levesque, G. A., and Vitello, P., 2015, “The Effect of Pore Morphology on Hot Spot Temperature,” Propellants, Explosives, Pyrotechnics, **40**(2), pp. 303–308.

[11] Tran, L., and Udaykumar, H. S., 2006, “Simulation of Void Collapse in an Energetic Material, Part 2: Reactive Case,” Journal of propulsion and power, **22**(5), pp. 959–974.

[12] Kapila, A. K., Schwendeman, D. W., Gambino, J. R., and Henshaw, W. D., 2015, “A Numerical Study of the Dynamics of Detonation Initiated by Cavity Collapse,” Shock Waves, pp. 1–28.

[13] Rai, N. K., Kapahi, A., and Udaykumar, H. S., 2014, “Treatment of Contact Separation in Eulerian High-Speed Multimaterial Dynamic Simulations,” Int. J. Numer. Meth. Engng, **100**(11), pp. 793–813.

[14] Levesque, G., Vitello, P., and Howard, W. M., 2013, “Hot-Spot Contributions in Shocked High Explosives from Mesoscale Ignition Models,” Journal of Applied Physics, **113**(23), p. 233513.

[15] Rai, N. K., and Udaykumar, H. S., 2015, “Mesoscale Simulation of Reactive Pressed Energetic Materials under Shock Loading,” Journal of Applied Physics, **118**(24), p. 245905.

[16] Eason, R. M., and Sewell, T. D., 2015, “Molecular Dynamics Simulations of the Collapse of a Cylindrical Pore in the Energetic Material α-RDX,” Journal of Dynamic Behavior of Materials, **1**(4), pp. 423–438.

[17] Zhou, T., Lou, J., Zhang, Y.-G., Song, H.-J., and Huang, F.-L., 2016, “Hot Spot Formation and Chemical Reaction Initiation in Shocked HMX Crystal with a Nanovoid: A Large-Scale Reactive Molecular Dynamics Study,” Physical Chemistry Chemical Physics.

[18] Tarver, C. M., and Tran, T. D., 2004, “Thermal Decomposition Models for HMX-Based Plastic Bonded Explosives,” Combustion and Flame, **137**(1), pp. 50–62.

[19] Sambasivan, S., Kapahi, A., and Udaykumar, H. S., 2012, “Simulation of High Speed Impact, Penetration and Fragmentation Problems on Locally Refined Cartesian Grids,” Journal of Computational Physics.

[20] Kapahi, A., Sambasivan, S., and Udaykumar, H. S., 2013, “A Three-Dimensional Sharp Interface Cartesian Grid Method for Solving High Speed Multi-Material Impact, Penetration and Fragmentation Problems,” Journal of Computational Physics, **241**, pp. 308–332.

[21] Kapahi, A., Mousel, J., Sambasivan, S., and Udaykumar, H. S., 2013, “Parallel, Sharp Interface Eulerian Approach to High-Speed Multi-Material Flows,” Computers & Fluids, **83**, pp. 144–156.

[22] Osher, S., 1988, “Fronts Propagating with Curvature Dependent Speed Algorithms Based on Hamilton-Jacobi Formulations,” Journal of Computational Physics, **79**, pp. 12–49.

[23] Fedkiw, R. P., Aslam, T., Merriman, B., and Osher, S., 1999, “A Non-Oscillatory Eulerian Approach to Interfaces in Multimaterial Flows (the Ghost Fluid Method),” J Comput Phys, **152**(2), pp. 457–492.

[24] Menikoff, R., and Sewell, T. D., 2002, “Constituent Properties of HMX Needed for Mesoscale Simulations,” Combustion theory and modelling, **6**(1), pp. 103–125.

[25] Tarver, C. M., Chidester, S. K., and Nichols, A. L., 1996, “Critical Conditions for Impact-and Shock-Induced Hot Spots in Solid Explosives,” The Journal of Physical Chemistry, **100**(14), pp. 5794–5799.

[26] Welle, E. J., Molek, C. D., Wixom, R. R., and Samuels, P., 2014, “Microstructural Effects on the Ignition Behavior of HMX,” *Journal of Physics: Conference Series*, IOP Publishing, p. 052049.

[27] Rai, N. K., Schmidt, M., and UdayKumar, H. S., “Collapse of Elonagted Voids in Porous Energetic Materials: Effect of Void Orientation and Aspect Ratio on Initiation,” Physical Review Fluids (Submitted).

[28] Kulikovskii, A. G., Pogorelov, N. V., and Semenov, A. Y., 2000, *Mathematical Aspects of Numerical Solution of Hyperbolic Systems*, CRC Press.

[29] Sewell, T. D., and Menikoff, R., 2003, “COMPLETE EQUATION OF STATE FOR/3-HMX AND IMPLICATIONS FOR INITIATION,” *Shock Compression of Condensed Matter-2003: Proceedings of the Conference of the American Physical Society, Topical Group on Shock Compression of Condensed Matter*, American Institute of Physics, p. 157.

[30] Ponthot, J.-P., 2002, “Unified Stress Update Algorithms for the Numerical Simulation of Large Deformation Elasto-Plastic and Elasto-Viscoplastic Processes,” International Journal of Plasticity, **18**(1), pp. 91–126.

[31] Shu, C.-W., and Osher, S., 1989, “Efficient Implementation of Essentially Non-Oscillatory Shock-Capturing Schemes, II,” Journal of Computational Physics, **83**(1), pp. 32–78.

[32] Strang, G., 1968, “On the Construction and Comparison of Difference Schemes,” SIAM Journal on Numerical Analysis, **5**(3), pp. 506–517.

[33] Fehlberg, E., 1968, *Classical Fifth-, Sixth-, Seventh-, and Eighth-Order Runge-Kutta Formulas with Stepsize Control*, National Aeronautics and Space Administration.

[34] Springer, H., Tarver, C., and Bastea, S., 2015, “Effects of High Shock Pressures and Pore Morphology.”

[35] Berger, M. J., and Colella, P., 1989, “Local Adaptive Mesh Refinement for Shock Hydrodynamics,” Journal of computational Physics, **82**(1), pp. 64–84.

Void Collapse Simulations	**Void Shape**	**Number of points across diameter**
Menikoff [6]	Cylindrical	100
Tran et. al. [7]	Cylindrical	100
Kapahi and Udaykumar [8]	Cylindrical	150
Kapila et. al. [12]	Spheroid	1000

Table I: Grid resolution used in the previous void collapse simulations.

$\rho_0(kg/m^3)$	1900
$K_0(GPa)$	16.5
$K_0^{'}$	8.7
a	1.1
b	-0.2
$c_0(K.kg/MJ)$	5.2653675×10^{-1}
$c_1(K.kg/MJ)$	3.0733581×10^{2}
$c_2(K.kg/MJ)$	1.8318931×10^{5}
$c_3(K.kg/MJ)$	4.1941409×10^{2}
$G(GPa)$	12
$Yield\ Stress\,(GPa)$	0.26
$\eta(GPa.\mu s)$	0.11
$T_{m0}(K)$	552

Table II: Constitutive properties of HMX [24,29] used in the current meso-scale analysis.

$\ln Z_1 \left(s^{-1}\right)$	48.7
$\ln Z_2 \left(s^{-1}\right)$	37.3
$\ln Z_3 \left(s^{-1}\right)$	28.1
$E_1 (kcal/m)$	52.7
$E_2 (kcal/m)$	44.1
$E_3 (kcal/m)$	34.1
$Q_1 (cal/g)$ at 298 K	+100
$Q_2 (cal/g)$ at 298 K	-300
$Q_3 (cal/g)$ at 298 K	-1200

Table III: HMX chemical reaction parameters for Tarver 3-equation [25] model.

Property	**HMX**	**fragments**	**Intermediate Gases**	**Final Gases**
Specific Heat, C_P(cal/ (g.K))				
293 K	0.24	0.22	0.24	0.27
433 K	0.34	0.31	0.27	0.28
533 K	0.40	0.36	0.29	0.29
623 K	0.46	0.42	0.31	0.30
773 K	0.55	0.50	0.35	0.31
$>$ 1273 K	0.55	0.50	0.42	0.35
Thermal Conductivity, λ (cal/(cm.s.K)				
293 K	1.23×10^{-3}	6.5×10^{-4}	1×10^{-4}	1×10^{-4}
433 K	9.7×10^{-4}	5.0×10^{-4}	1×10^{-4}	1×10^{-4}
533 K	8.1×10^{-4}	4.0×10^{-4}	1×10^{-4}	1×10^{-4}
$>$ 623 K	7.0×10^{-4}	3.0×10^{-4}	1×10^{-4}	1×10^{-4}

Table IV: Specific heat and thermal conductivity for all the four species from the Tarver 3-equation [25] model for various temperatures.

Simulation	Bulk Temperature (K)	Material jet speed during the first collapse (m/s)	Temperature reached after the collapse (K)
Springer et al. [34]	925	7.4	>4000
SCIMITAR3D	944	7.2	4400

Table V: Comparison of void collapse simulation results obtained from Springer et al. [34] analysis on spherical void and SCIMITAR3D cylindrical void for shock speed of $25GPa$ and void diameter of $1\mu m$

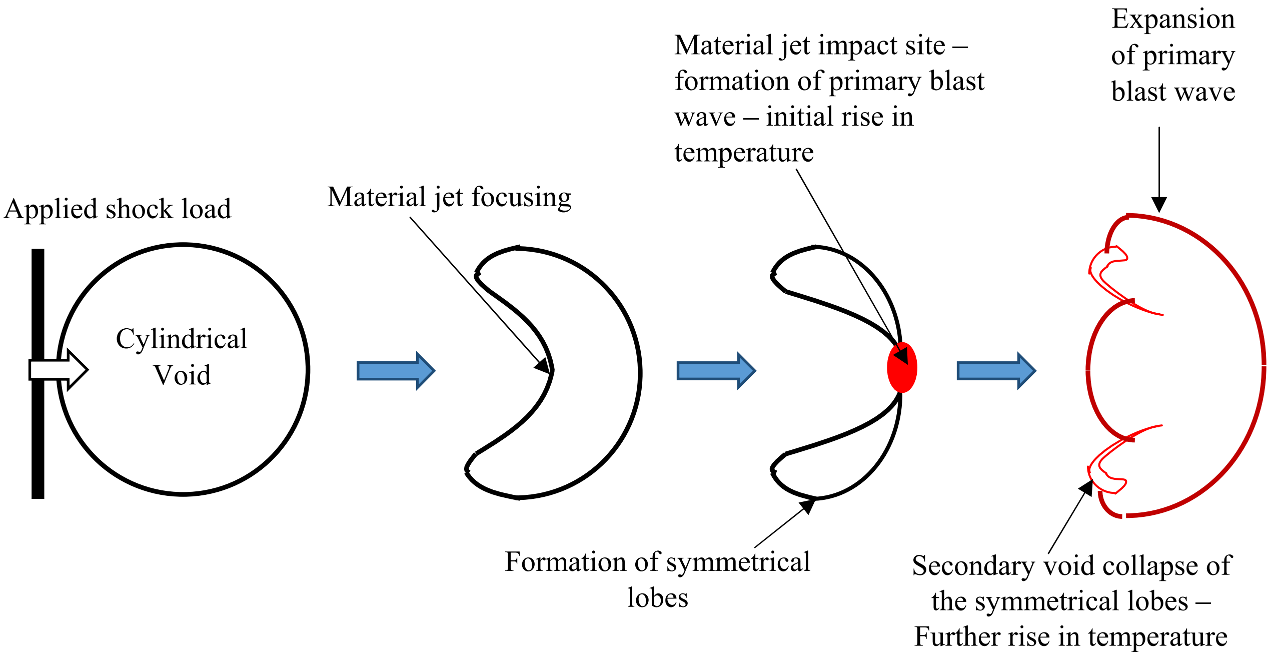

Figure 1: Schematic representation of the different stages involved in the collapse of a cylindrical void under the applied shock load.

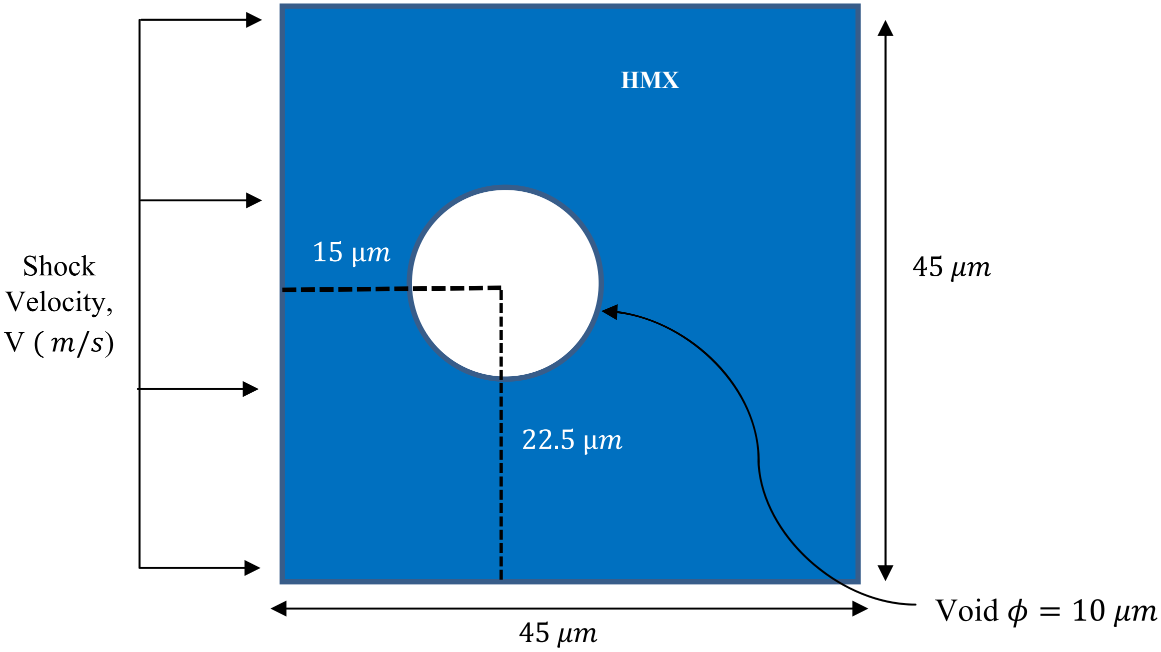

Figure 2: A cylindrical void of diameter 10 µm embedded in the HMX domain of size 45 µm × 45 µm. Shock load is applied as a velocity boundary condition in the form of a pulse of duration 3 ns. The east, south and north faces of the domain are supplied with outlet boundary condition.

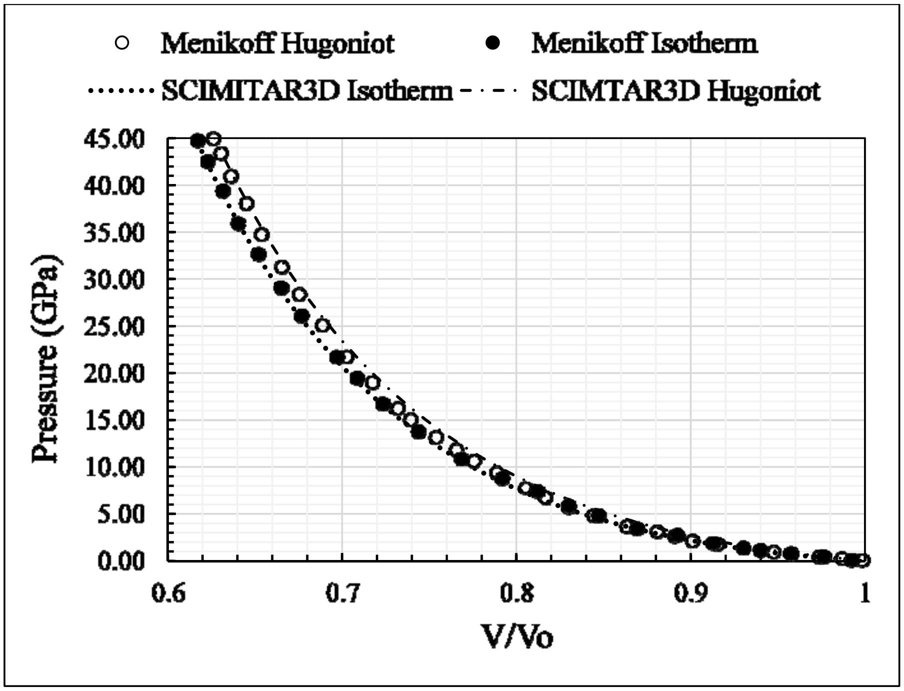

(a) Comparison of Isotherm and Hugoniot for HMX with Menikoff et al. [29].

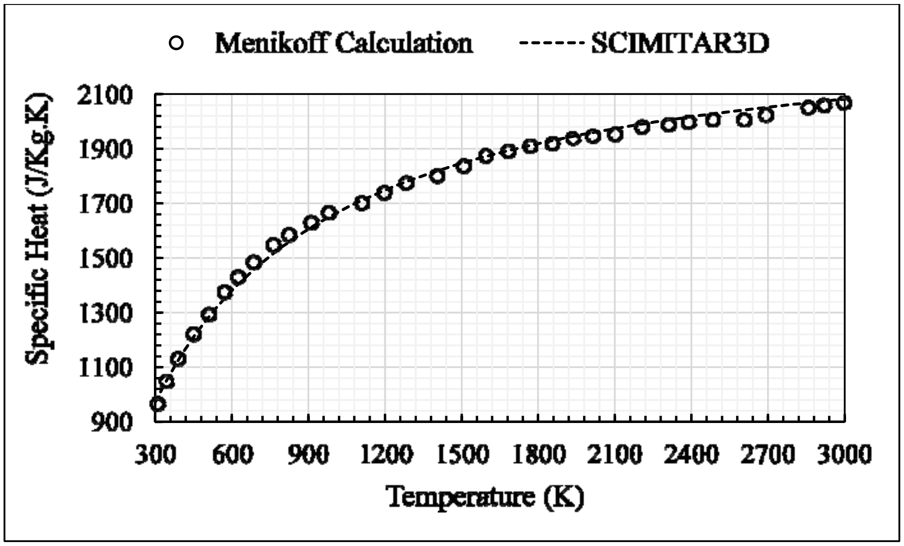

(b) Comparison of Specific Heat Variation with temperature for HMX with Menikoff et al. [29].

Figure 3: Verification of the current implementation of the HMX constitutive model. The current implementation for equation of state and specific heat is compared with the results from Menikoff et.al. [29]

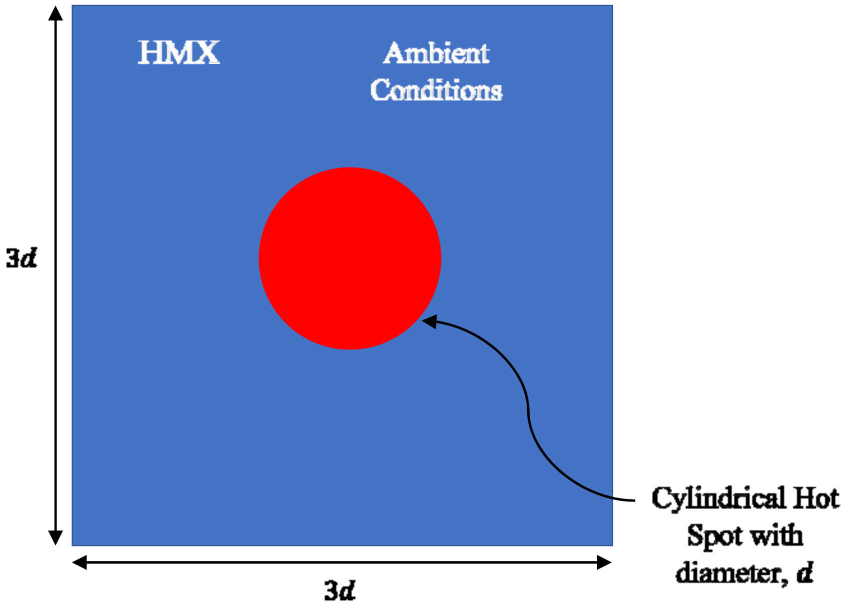

(a) A cylindrical hot spot with diameter, d in HMX matrix of size $3d \times 3d$. The hot spot is at an elevated temperature than the surroundings. The surrounding is kept at ambient temperature of 298 K.

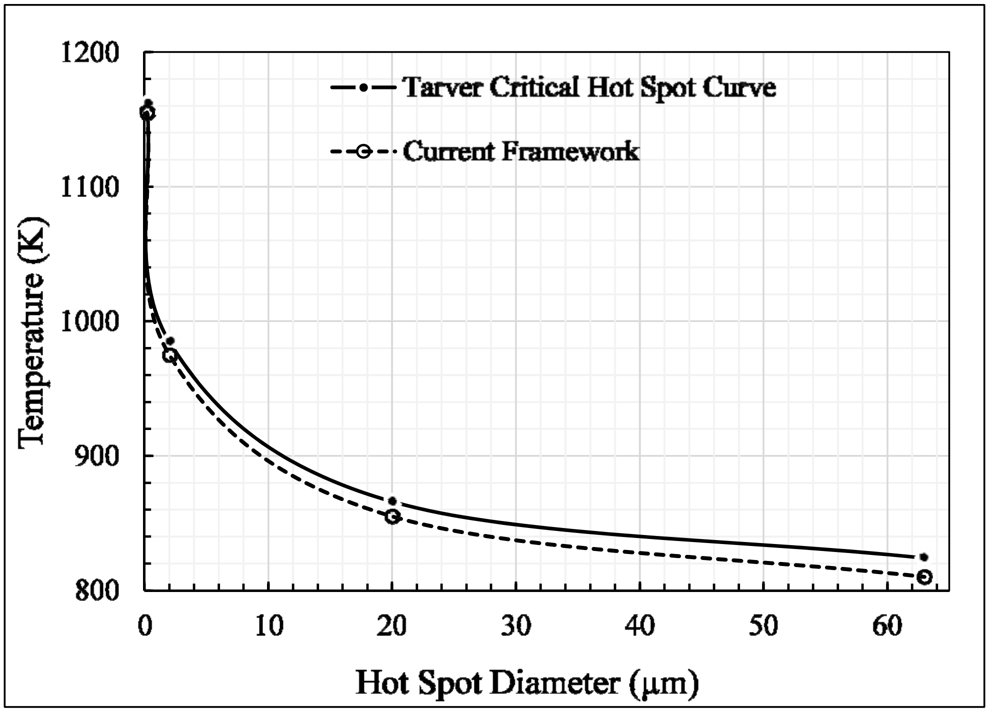

(b) Comparison of critical hot spot plot for HMX with Tarver et al. [25] results.

Figure 4: Verification of the implementation of the Tarver 3 step model in the current framework. The critical hot spot plot from the work of Tarver et al. is compared with the current results.

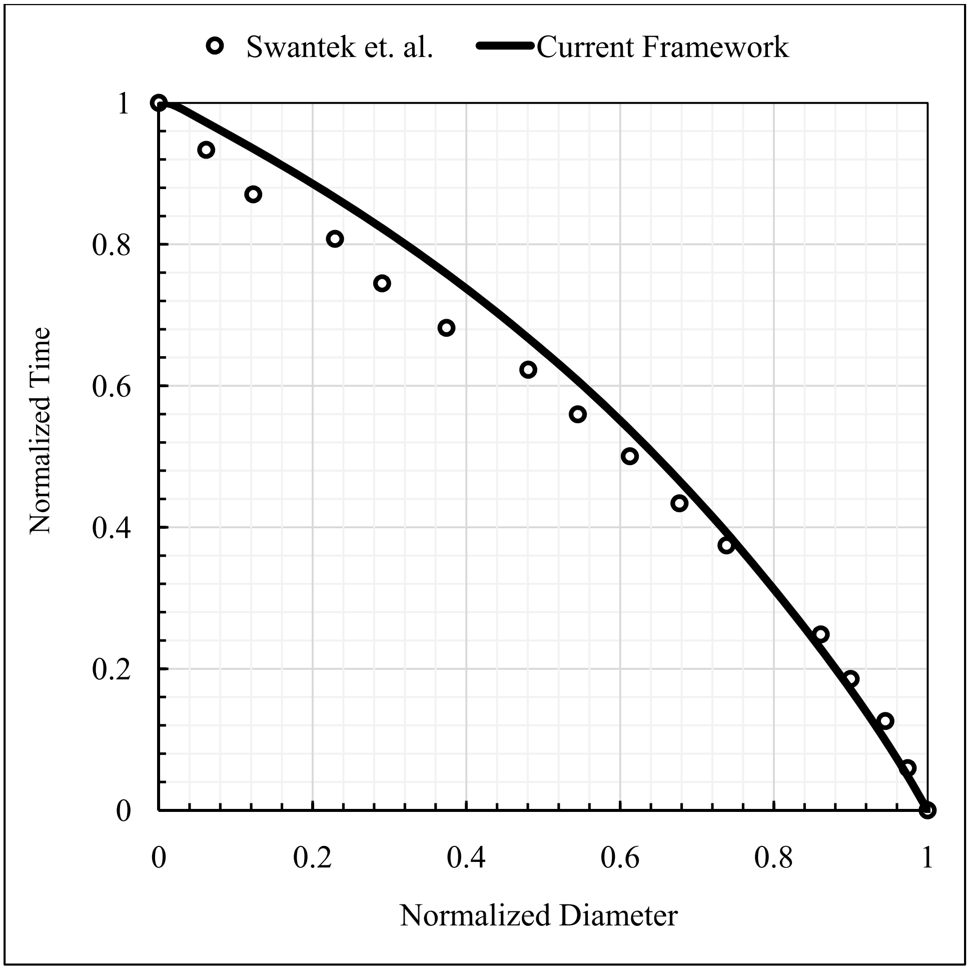

Figure 5: Comparison plot of normalized time vs normalized diameter between the current implementation and Swantek et al. [2] experimental result. The result shown is obtained by performing shock analysis with shock strength of $500\ m/s$ on a single cylindrical void in a HMX matrix. Normalized diameter is the ratio between the centerline diameter of the deformed void and the original diameter. Normalized time is the ratio between the current time when void deforms and total time for the complete closure of the void.

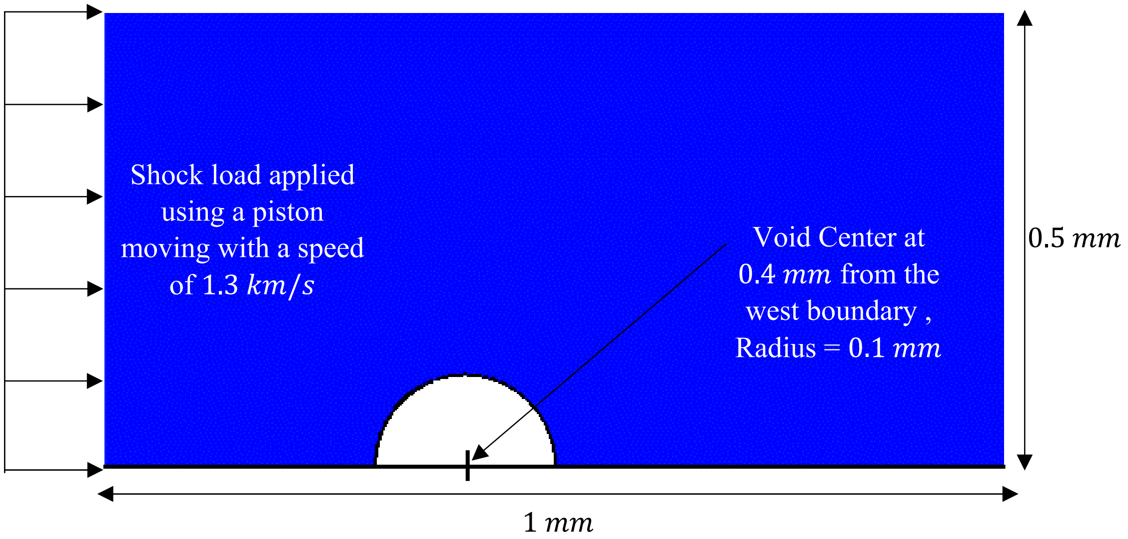

(a) Computational set up

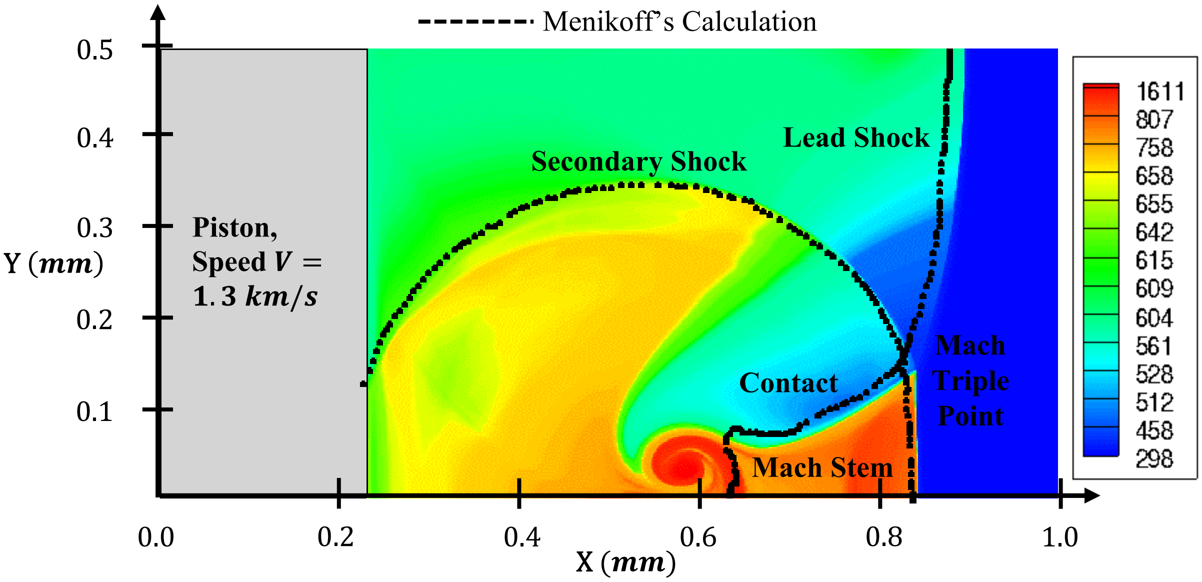

(b) Verification of inert void collapse analysis results with Menikoff's [6] calculations

Figure 6: Comparison of inert void collapse simulation analysis results with Menikoff's [6] calculations. Cylindrical void of radius 0.1 mm in HMX located at (0.4 mm, 0) is considered for analysis. A piston driving the shock wave at a particle speed of 1.3 km/s is applied at the west face of the domain boundary.

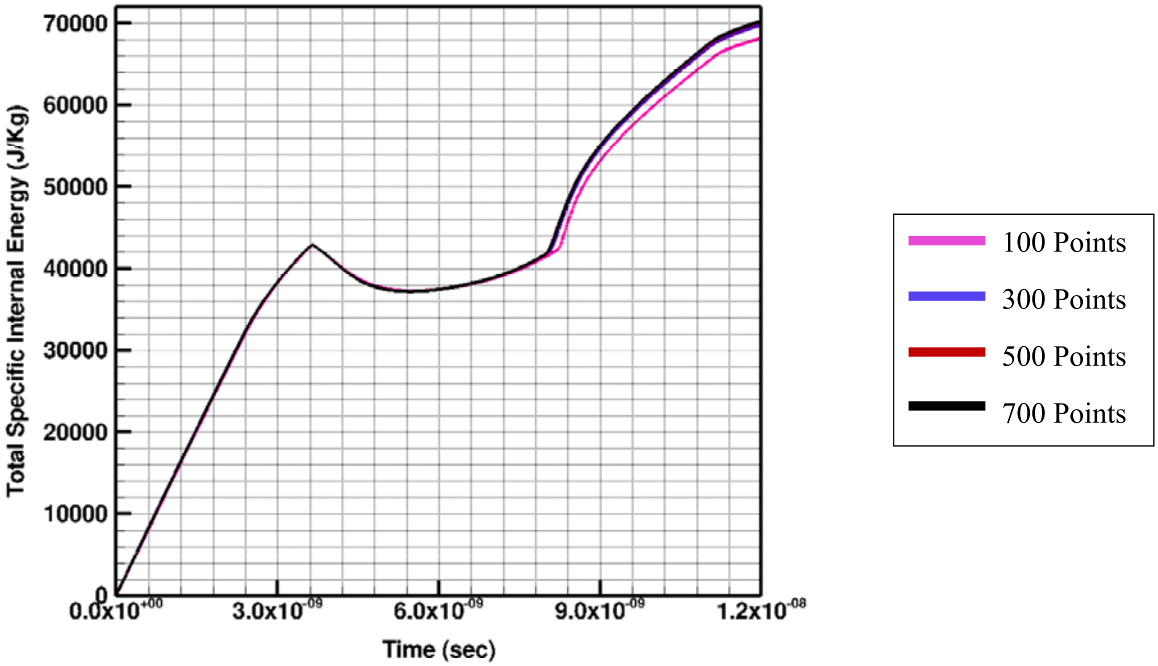

(a) Time Variation of total specific internal energy in the domain for 4 grid sizes

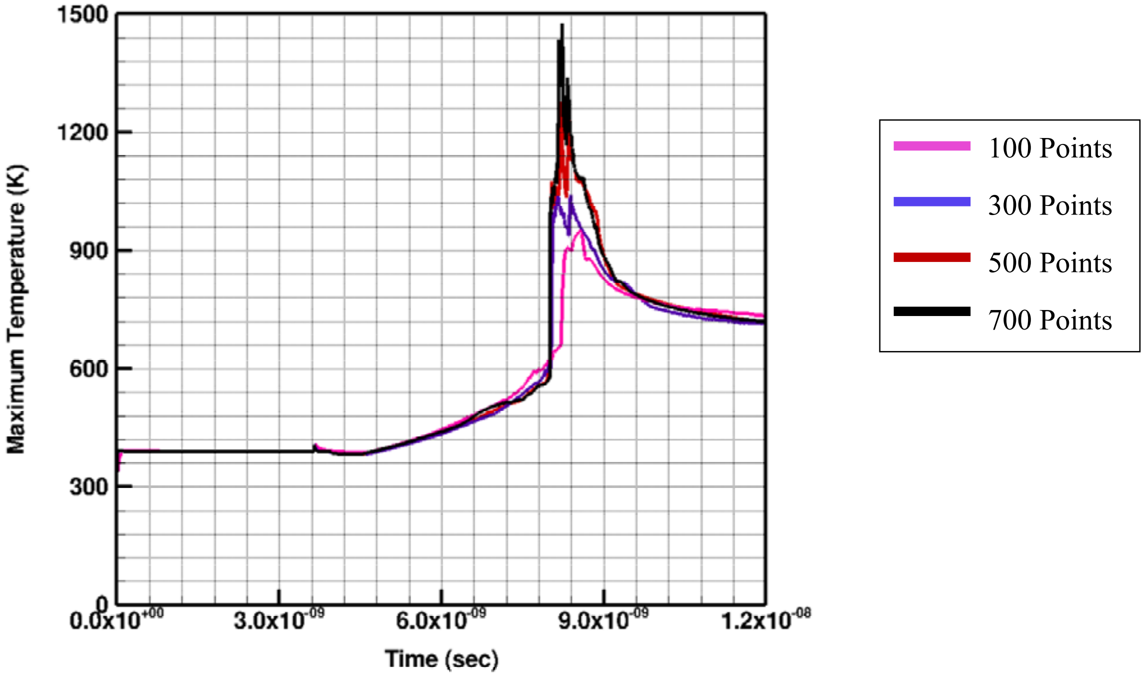

(b) Time Variation of maximum temperature in the domain for 4 grid sizes

Figure 7: Grid convergence study for the inert void collapse simulation. The study is performed for a single void of diameter 10 μm in HMX material under the shock loading of $500\ m/s$. Four different grid sizes corresponding to $100, 300, 500$ and 700 grid points across the void diameter are considered.

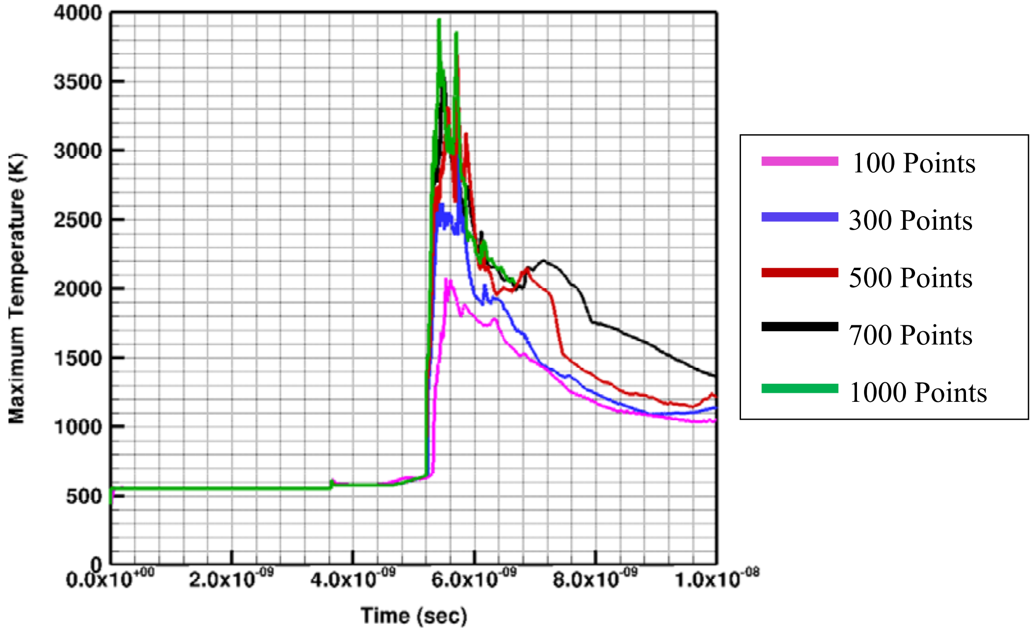

(a) Time Variation of maximum temperature in the domain for 5 grid sizes

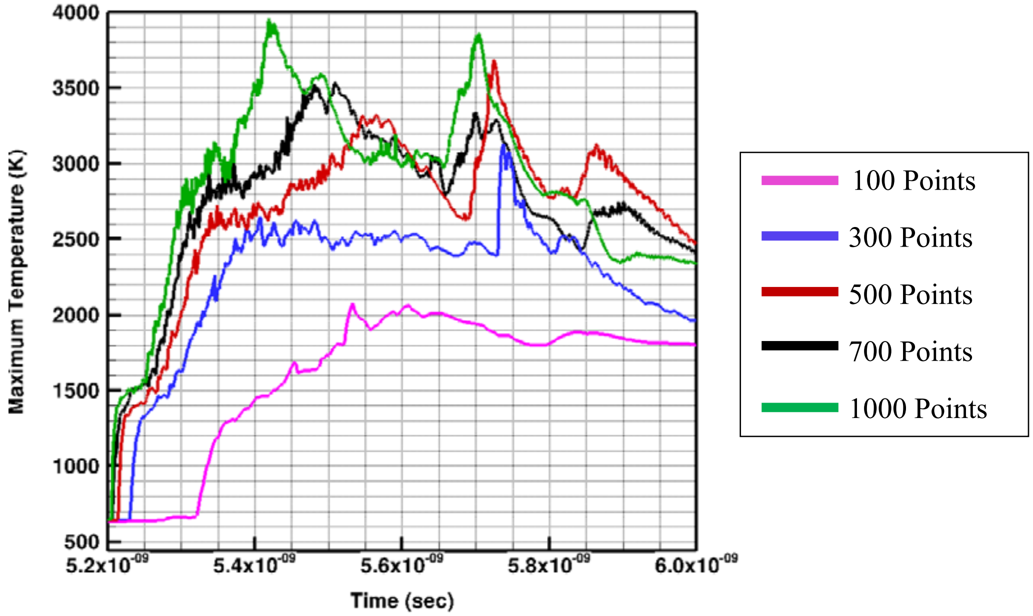

(a) Time variation of maximum temperature in the domain focusing on the secondary peaks of temperature. This plot is a zoomed view of plot

Figure 8: Grid convergence study for the inert void collapse simulation. The study is performed for a single void of diameter 10 μm in HMX material under the shock loading of 1000 m/s. Five different grid sizes corresponding to 100, 300, 500, 700 and 1000 grid points across the void diameter are considered.

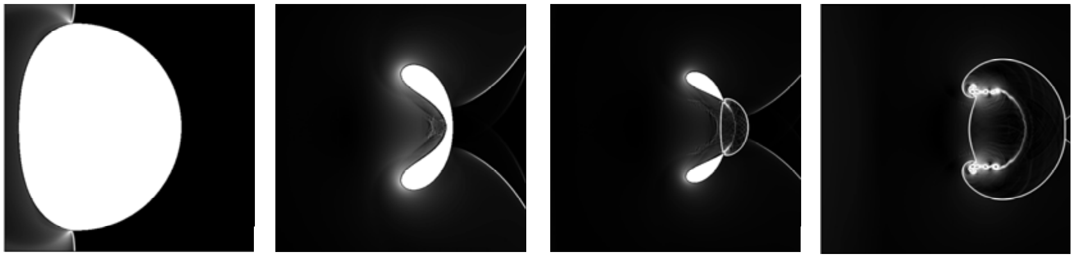

(a) Numerical Schlieren

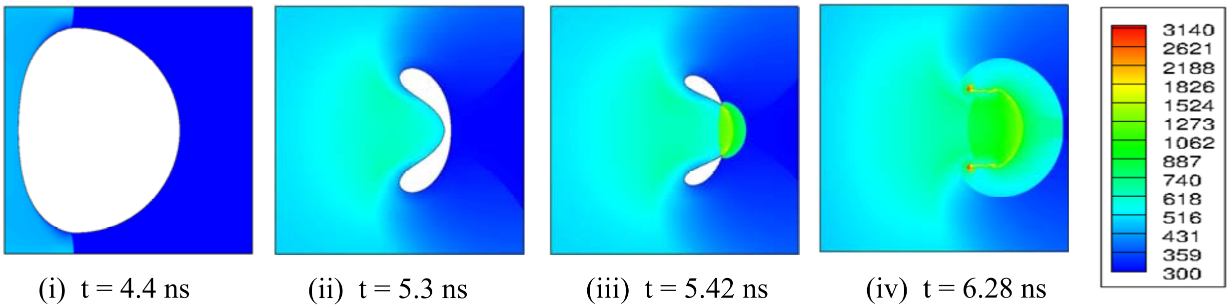

(i) t = 4.4 ns (ii) t = 5.3 ns (iii) t = 5.42 ns (iv) t = 6.28 ns

(b) Temperature contours (K)

Figure 9: Contour plots of numerical Schlieren and temperature at different instances of time for inert single void collapse analysis under shock loading of $1000\ m/s$. The grid size for the current simulation corresponds to 700 grid points across the void diameter of $10\ \mu m$.

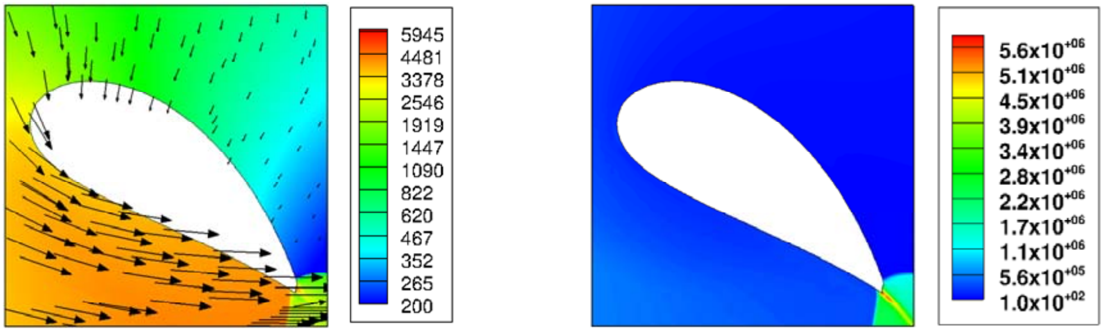

(a) Velocity Magnitude at t = 3.54 ns (b) Total Specific Internal Energy at t = 3.54 ns

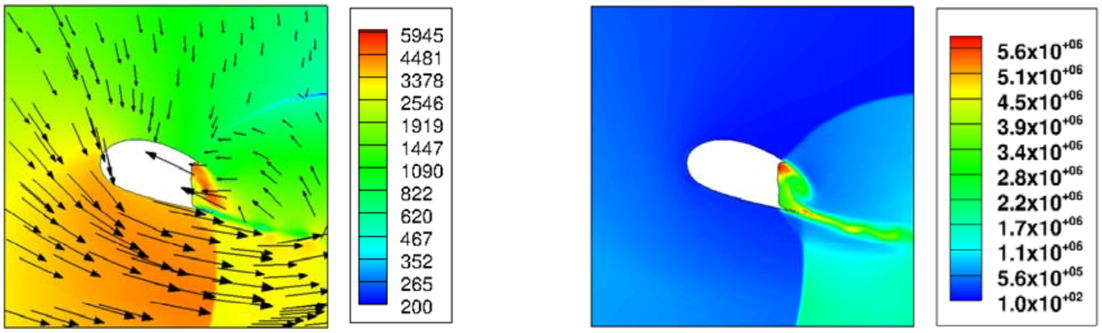

(c) Velocity Magnitude at t = 3.93 ns (d) Total Specific Internal Energy at t = 3.93 ns

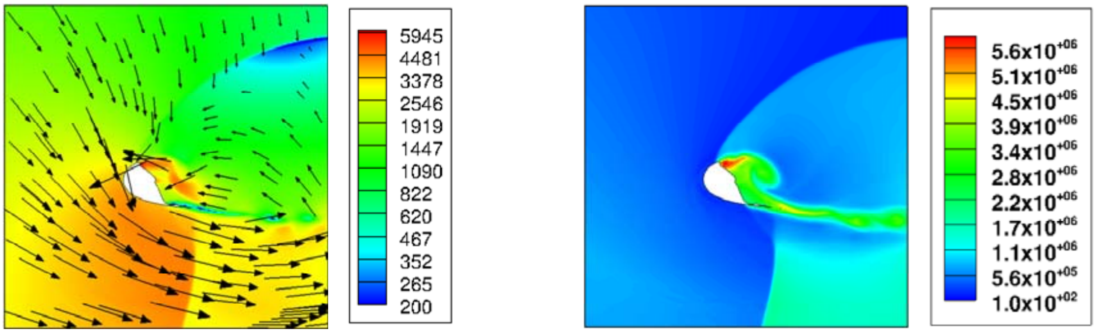

(e) Velocity Magnitude at t = 4.094 ns (f) Total Specific Internal Energy at t = 4.094 ns

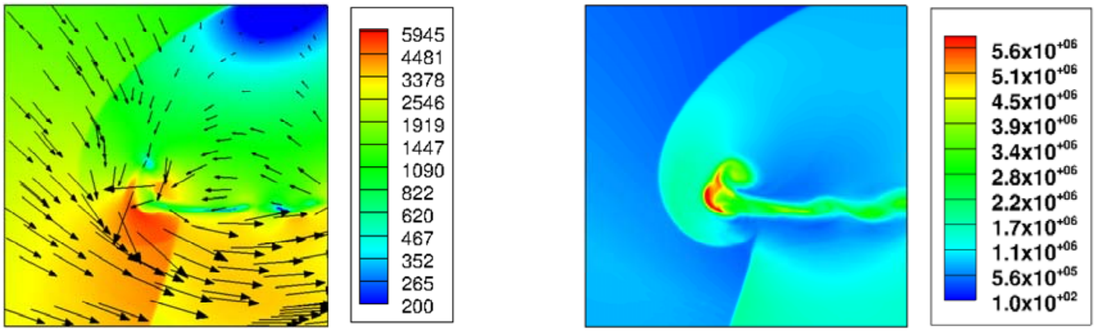

(g) Velocity Magnitude at t = 4.33 ns (h) Total Specific Internal Energy at t = 4.33 ns

Figure 10: Contour plots of the magnitude of the total velocity(m/s) and total specific internal energy(J/Kg) at different instants of time for inert single void collapse analysis under shock loading of 1000 m/s. The grid size for the current simulation corresponds to 700 grid points across the void diameter of 10 μm.

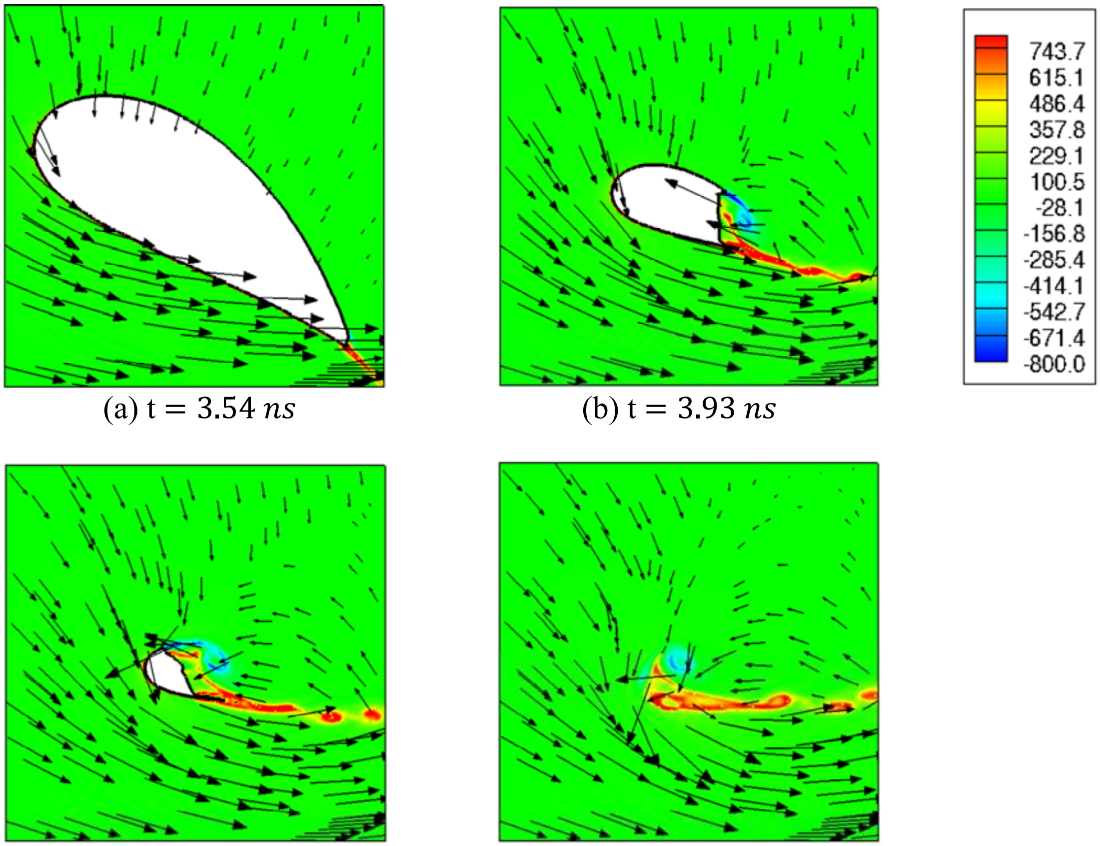

(a) t = 3.54 ns (b) t = 3.93 ns

(c) t = 4.094 ns (d) t = 4.33 ns

Figure 11: Contour plots of vorticity near the collapse of the secondary lobes for the shock speed of 1000 m/s. The grid size for the current simulation corresponds to 700 grid points across the void diameter of 10 μm. The plot is shown for one of the secondary lobes obtained by the initial jet impact.

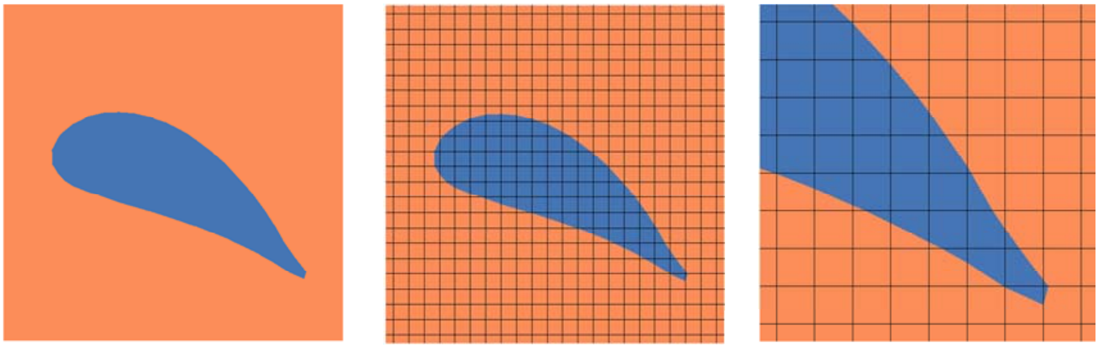

(a) Shape of the secondary lobe under coarse grid (100 points across the initial void diameter)

(b) Grid size for the under resolved secondary lobe

(c) Resolution of lobe tip

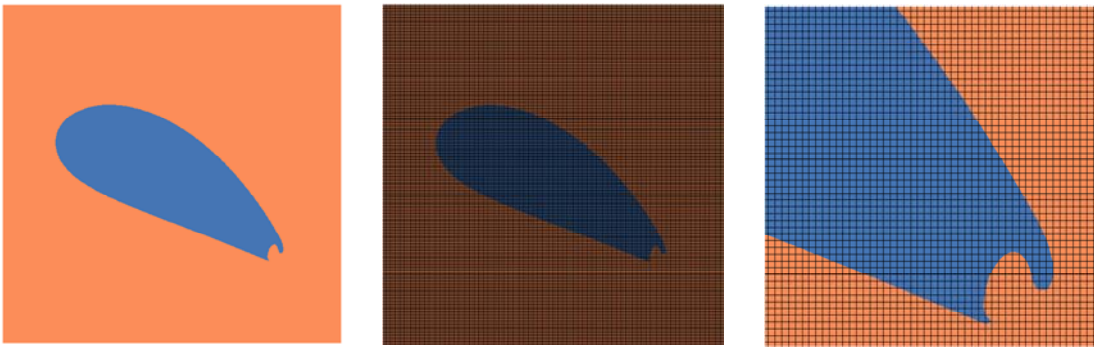

(d) Shape of the secondary lobe under coarse grid (700 points across the initial void diameter)

(e) Grid resolution for the well resolved secondary lobe

(f) Well resolved lobe tip

Figure 12: Comparison of the shape of one of the secondary lobes for the coarsest grid i.e. 100 points across the cylinder diameter and the finest grid i.e. 700 grid points across the cylinder diameter. The cylinder diameter is 10 μm. The shape of the secondary lobe is shown for the time instance corresponding to the time just after the initial jet impact. The lobe is unresolved for the coarse grid and is smaller as compared to the finer grid.

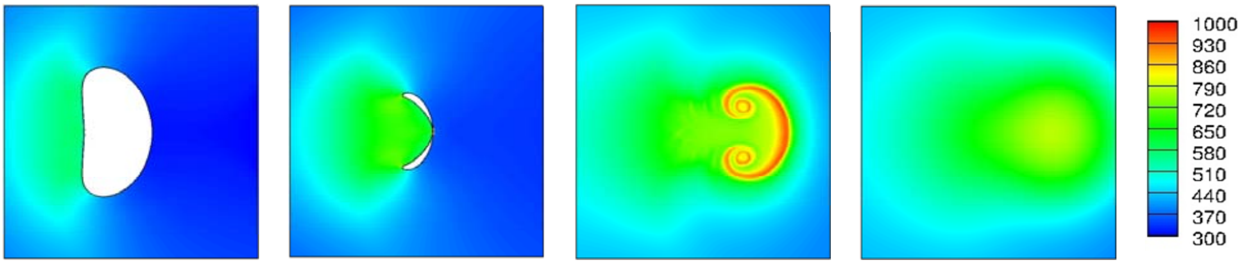

(a) Temperature contours (K)

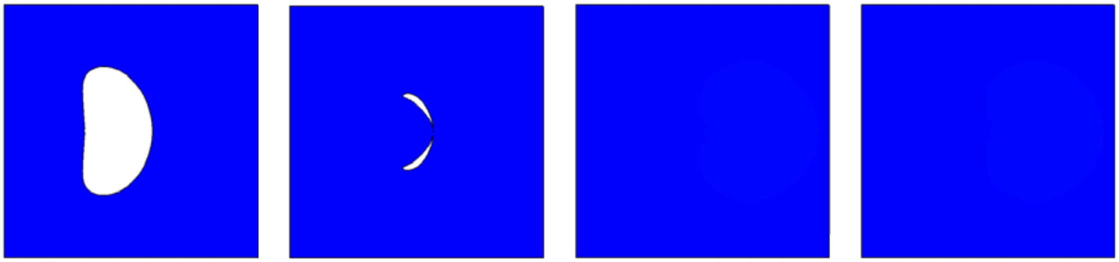

(i) t = 6.9 ns (ii) t = 8.1 ns (iii) t = 10.18 ns (iv) t = 9.06 µs

(b) Final species mass fraction. No reaction is observed and the mass fraction is zero.

Figure 13: Contour plots of temperature and mass fraction of the final species at different instances of time for reactive single void collapse analysis under shock loading of $500\ m/s$. The grid size for the current simulation corresponds to 700 grid points across the void diameter of $10\ \mu m$. No reaction is observed for the current shock strength.

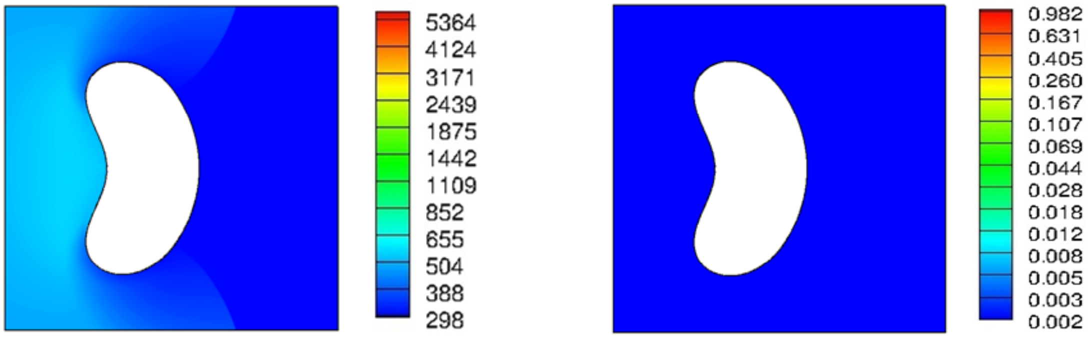

(a) Temperature (K) at t = 4.41 ns (b) Final species mass fraction at t = 4.41 ns

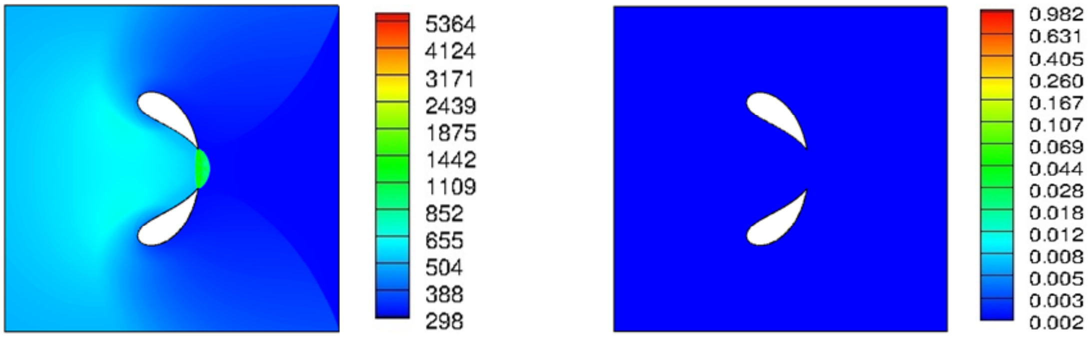

(c) Temperature (K) at t = 5.26 ns (d) Final species mass fraction at t = 5.26 ns

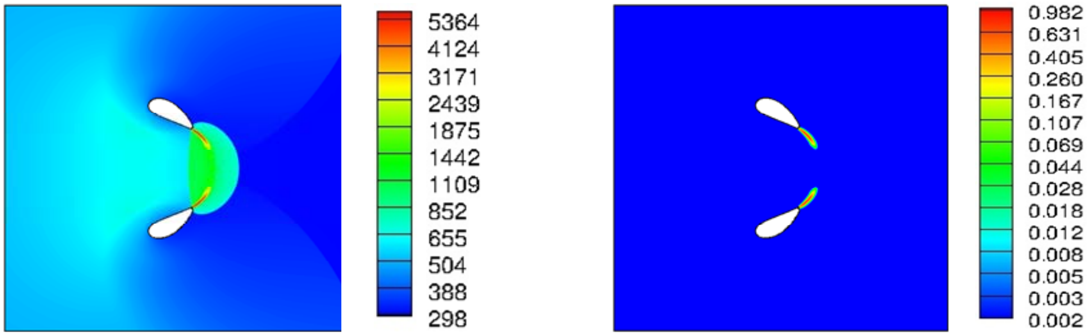

(e) Temperature (K) at t = 5.41 ns (f) Final species mass fraction at t = 5.41 ns

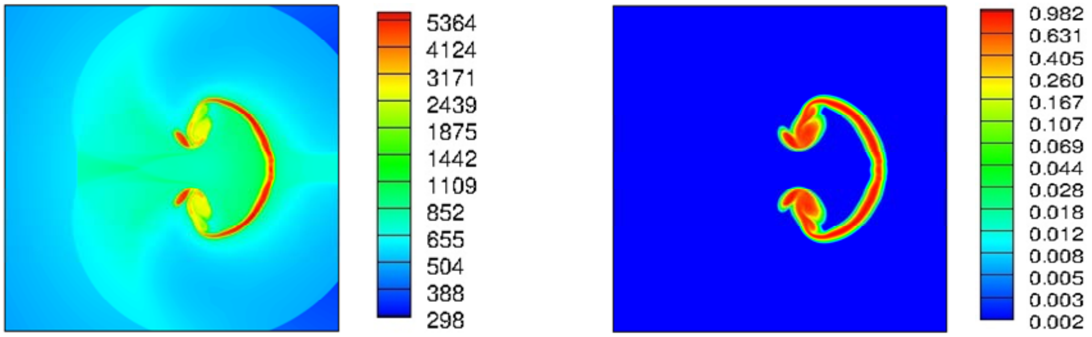

(g) Temperature (K) at t = 6.28 ns (h) Final species mass fraction at t = 6.28 ns

Figure 14: Contour plots of temperature and mass fraction of the final species at different instances of time for reactive single void collapse analysis under shock loading of 1000 m/s. The grid size for the current simulation corresponds to 700 grid points across the void diameter of 10 μm.Reaction initiates away from the initial jet impact. Therefore, high resolution is required for the accurate prediction of the secondary peaks.

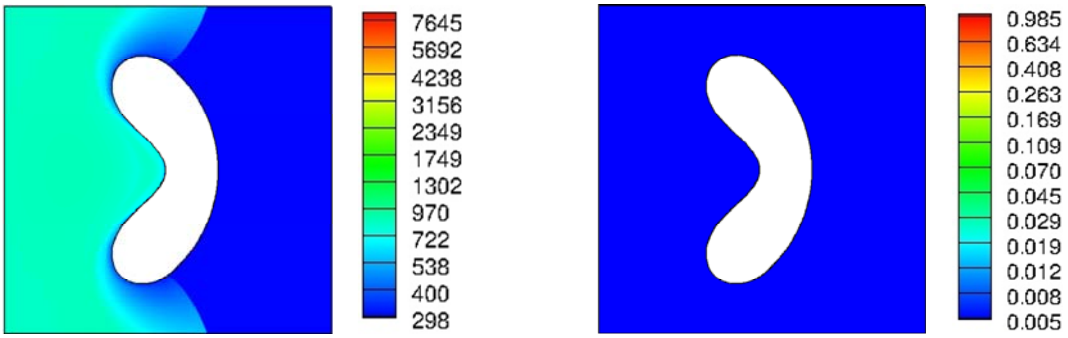

(a) Temperature (K) at t = $3.54\ ns$ (b) Final Species mass fraction at t = $3.54\ ns$

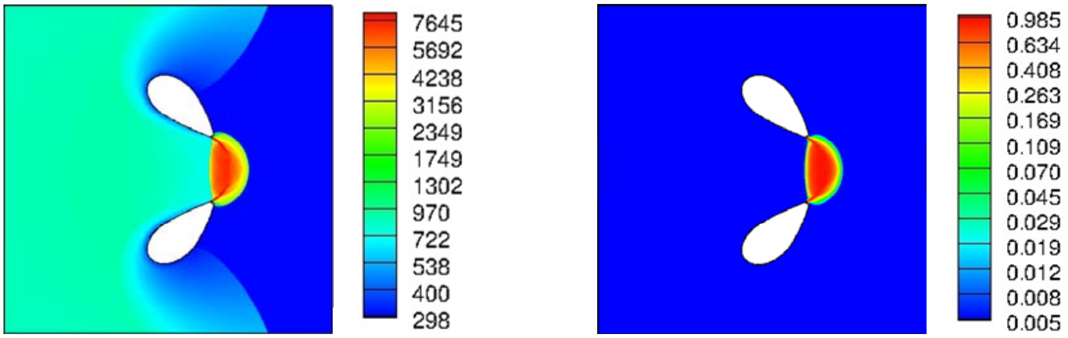

(c) Temperature (K) at t = $3.93\ ns$ (d) Final Species mass fraction at t = $3.93\ ns$

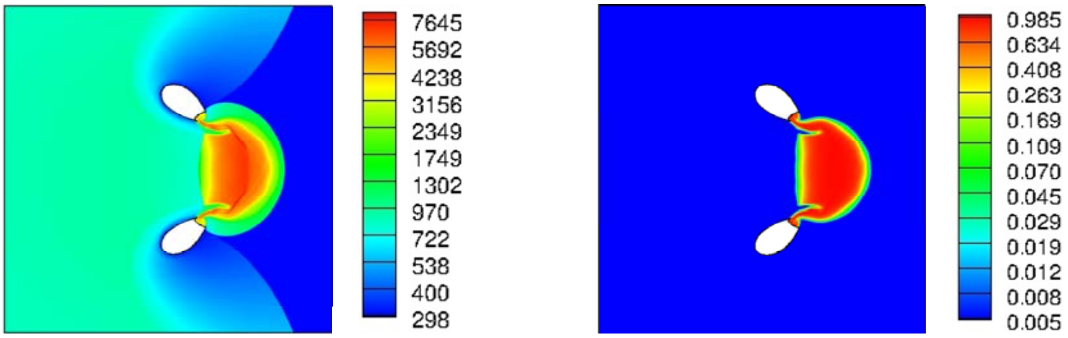

(e) Temperature (K) at t = $4.094\ ns$ (f) Final Species mass fraction at t = $4.094\ ns$

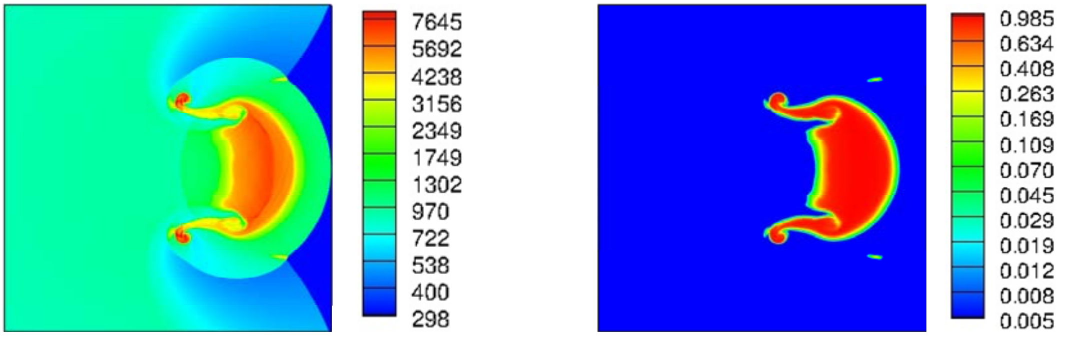

(g) Temperature (K) at t = $4.33\ ns$ (h) Final Species mass fraction at t = $4.33\ ns$

Figure 15: Contour plots of temperature and mass fraction of the final species at different instances of time for reactive single void collapse analysis under shock loading of $2000\ m/s$. The grid size for the current simulation corresponds to 700 grid points across the void diameter of $10\ \mu m$.

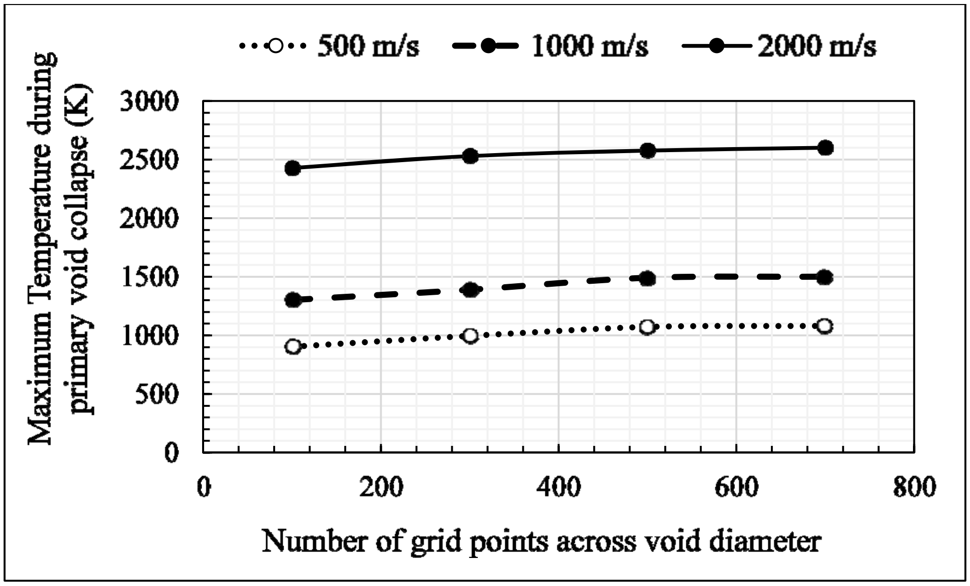

(a) Convergence plot for the maximum temperature reached during the primary void collapse after the test jet impact for different grid resolution.

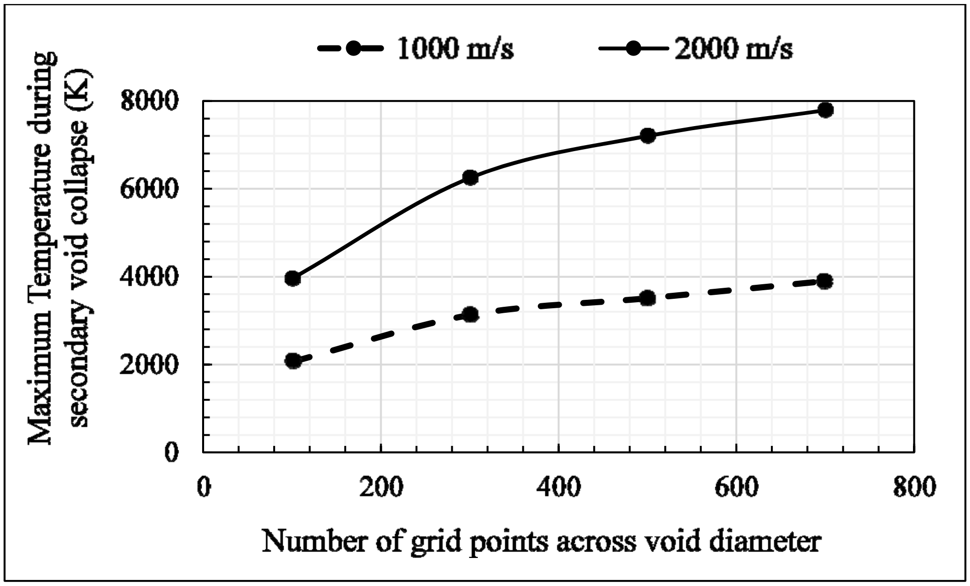

(b) Convergence plot for the maximum temperature reached during the secondary void collapse under the influence of blast wave formed during the initial jet impact.

Figure 16: Grid convergence plot for the maximum temperature achieved during the primary and secondary void collapse. Four different grid sizes are considered corresponding to $100, 300, 500$ and 700 grid points across void diameter of $10\ \mu m$.